universität wien

MASTERARBEIT | MASTER'S THESIS

Titel | Title

Hydrodynamics of Deformable Swimming Cells in MPCD Fluids

verfasst von | submitted by

Johannes Pichler BSc

angestrebter akademischer Grad | in partial fulfilment of the requirements for the degree of

Master of Science (MSc)

Wien | Vienna, 2026

Studienkennzahl lt. Studienblatt | Degree programme code as it appears on the student record sheet:	UA 066 876
Studienrichtung lt. Studienblatt | Degree programme as it appears on the student record sheet:	Masterstudium Physics
Betreut von | Supervisor:	DI Dr. Andreas Zöttl Privatdoz.

Acknowledgements

First and foremost, I would like to express my sincere gratitude to my supervisor, Andreas Zöttl, for his guidance and support throughout this thesis. He introduced me to the fascinating world of microswimmers and low Reynolds number hydrodynamics, and his patience in explaining concepts, his constructive feedback on my work, and his encouragement to explore new directions have been invaluable. I am grateful for the opportunity to work on this project under his supervision.

I am deeply thankful to my parents, who made it possible for me to attend university in the first place. Their unwavering support and belief in me have been the foundation upon which I could build my academic path.

Most of all, I want to thank my partner Nadine. She stood by my side throughout this entire journey, motivated me when progress felt slow, and encouraged me to keep going even when the work was hard. Her patience, understanding, and constant support mean more to me than words can express. This thesis would not have been possible without her.

Abstract

Biological cells and synthetic microswimmers must generate non-reciprocal body deformations to achieve locomotion in viscous environments where inertia is negligible. While theoretical models often assume rigid swimmers with prescribed surface velocities, real cells possess deformable membranes whose mechanical properties fundamentally influence swimming behavior. This thesis investigates how surface mechanics govern the locomotion of a deformable cell using coupled Molecular Dynamics and Multi-Particle Collision Dynamics (MPCD) simulations.

The cell is modeled as a triangulated elastic surface with 1002 nodes, incorporating interaction potentials for bond elasticity, bending rigidity, and volume conservation. The cell modell is immersed in an MPCD fluid that captures the essential hydrodynamics at low Reynolds number (Re ≈ 0.22). Non-reciprocal swimming is achieved through time-periodic forces applied to three surface nodes forming an equatorial triangle, with phase shifts that break time-reversal symmetry.

Systematic parameter studies reveal three central findings. First, the swimming velocity obeys the canonical microswimmer scaling relation $v \propto \varepsilon_2^2 f$, where ε_2 is the deformation amplitude and f the driving frequency, validated with high correlation ($R^2 = 0.98$). Second, surface bending rigidity controls both deformation amplitude and cell asphericity: stiffer cell surfaces remain more spherical and exhibit smaller deformations. Third, and most strikingly, bending rigidity determines swimming direction. Soft surfaces enable forward swimming through stroking-dominated propulsion, while stiff surfaces cause backward swimming where surface velocity effects dominate. The transition occurs at intermediate rigidity values ($k_{\mathrm{Bend}} = 1000$–$2000\, k_B T$).

These results demonstrate that cell surface mechanical properties offer a control mechanism for microswimmer locomotion, with implications for understanding biological cell motility and designing synthetic micro-robots with tunable swimming characteristics.

Zusammenfassung

Biologische Zellen und synthetische Mikroschwimmer müssen nicht-reziproke Körperverformungen erzeugen, um sich in viskosen Umgebungen fortzubewegen, in denen Trägheitseffekte vernachlässigbar sind. Während theoretische Modelle häufig starre Schwimmer mit vorgegebenen Oberflächengeschwindigkeiten annehmen, besitzen reale Zellen verformbare Membranen, deren mechanische Eigenschaften das Schwimmverhalten grundlegend beeinflussen. Diese Masterarbeit untersucht, wie die Membranmechanik die Fortbewegung einer verformbaren Zelle beeinflusst, mittels gekoppelter Molekulardynamik- und Multi-Particle Collision Dynamics (MPCD) Simulationen.

Die Zelle wird als triangulierte elastische Oberfläche mit 1002 Knoten modelliert, wobei Wechselwirkungspotentiale für Bindungselastizität, Biegesteifigkeit und Volumenerhaltung berücksichtigt werden. Das Zellenmodell ist in ein MPCD-Fluid eingebettet, das die wesentliche Hydrodynamik bei niedriger Reynoldszahl ($\mathrm{Re} \approx 0{,}22$) erfasst. Nicht-reziprokes Schwimmen wird durch zeitlich periodische Kräfte erreicht, die auf drei Oberflächennodes eines gleichseitigen Dreiecks wirken, wobei Phasenverschiebungen die Zeitumkehrsymmetrie brechen.

Systematische Parameterstudien liefern drei zentrale Ergebnisse. Erstens folgt die Schwimmgeschwindigkeit der kanonischen Skalierungsrelation für Mikroschwimmer $v \propto \varepsilon_2^2 f$, wobei ε_2 die Verformungsamplitude und f die Antriebsfrequenz bezeichnet; dies wurde mit hoher Korrelation ($R^2 = 0{,}98$) bestätigt. Zweitens beeinflusst die Biegesteifigkeit der Oberfläche sowohl die Verformungsamplitude als auch die Asphärizität der Zelle: steifere Oberflächen bleiben sphärischer und zeigen geringere Verformungen. Drittens, und besonders bemerkenswert, bestimmt die Biegesteifigkeit die Schwimmrichtung. Weiche Oberflächen ermöglichen Vorwärtsschwimmen durch schlagdominierten Antrieb, während steife Oberflächen Rückwärtsschwimmen verursachen, bei dem Oberflächengeschwindigkeitseffekte dominieren. Der Übergang erfolgt bei mittleren Steifigkeitswerten ($k_{\mathrm{Bend}} = 1000$–$2000\, k_B T$).

Diese Ergebnisse zeigen, dass die mechanischen Eigenschaften der Oberfläche einen Kontrollmechanismus für die Fortbewegung von Mikroschwimmern darstellen. Dies hat Implikationen sowohl für das Verständnis biologischer Zellmotilität als auch für die Entwicklung synthetischer Mikroroboter mit einstellbaren Schwimmeigenschaften.

Contents

1. Introduction

1.1. Biological Motivation

The ability of cells to move through their environment is fundamental to numerous biological processes. From immune cells navigating through tissues to hunt pathogens [1], [2], to metastatic cancer cells migrating through the extracellular matrix [3], [4], cellular motility underlies both physiological function and disease progression. Understanding the physical mechanisms that enable cell locomotion is therefore of paramount importance for biology and medicine.

Cells employ a remarkable variety of locomotion strategies depending on their environment and biological function. Amoeboid cells such as *Dictyostelium discoideum* and neutrophils crawl along surfaces through cycles of protrusion and retraction [5], [6], while sperm cells [7] and many bacteria [8], [9] propel themselves through bulk fluid using whip-like flagella. Between these extremes lies a rich spectrum of motility modes, including ciliary beating [10], [11], blebbing, and coordinated surface deformations.

A unifying feature of all cellular locomotion is that it occurs at microscopic length scales where the physics of fluid flow differs dramatically from our everyday macroscopic experience. Cells typically range from 1 to 100 micrometers in size. Swimming microorganisms such as bacteria and sperm move at speeds of micrometers per second [12], [13], while most mammalian cells migrate by crawling at speeds of micrometers per minute [14]. At these scales, viscous forces completely dominate over inertia, placing severe constraints on the types of motion that can produce net displacement. This regime, known as low Reynolds number hydrodynamics, demands specialized locomotion strategies that have evolved independently across diverse branches of life.

Despite decades of research on microswimmer hydrodynamics, significant gaps remain in our understanding of how deformable, membrane-bound cells achieve locomotion. Most theoretical and computational studies have focused either on rigid swimmers with prescribed surface velocities (such as the squirmer model) or on specific biological structures like bacterial flagella [15]. The intermediate case, a compliant cell body that swims through coordinated deformation of its own surface, remains comparatively unexplored. This thesis addresses this gap by developing and analyzing a computational model for deformable cell swimming, investigating how membrane mechanical properties govern locomotion performance.

1.2. Hydrodynamics at Low Reynolds Numbers

1.2.1. The Navier-Stokes Equations

The motion of viscous fluids is governed by the Navier-Stokes equations, which express conservation of momentum for a continuous fluid medium. For an incompressible Newtonian fluid with density ρ and dynamic viscosity η, the momentum equation takes the form

$$\rho\left(\frac{\partial \mathbf{v}}{\partial t} + (\mathbf{v}\cdot\nabla)\mathbf{v}\right) = -\nabla p + \eta\nabla^2\mathbf{v} + \mathbf{f}, \tag{1.1}$$

where $\mathbf{v}(\mathbf{r},t)$ is the fluid velocity field, $p(\mathbf{r},t)$ is the pressure, and $\mathbf{f}$ represents external body forces. The left-hand side contains the inertial terms: the local acceleration $\partial\mathbf{v}/\partial t$ and the convective acceleration $(\mathbf{v}\cdot\nabla)\mathbf{v}$. The right-hand side contains the forces per unit volume acting on each fluid element: the pressure gradient, viscous stresses, and external forces.

The incompressibility condition requires that the velocity field be divergence-free:

$$\nabla\cdot\mathbf{v} = 0. \tag{1.2}$$

Together, Equations (1.1) and (1.2) form a closed system that, in principle, determines the fluid motion for any given boundary conditions and external forcing. The mathematical structure and physical interpretation of these equations are discussed extensively in classic texts such as "Fluid Mechanics" by Landau and Lifshitz [16].

1.2.2. The Reynolds Number

The relative importance of inertial and viscous effects in a fluid flow is characterized by the Reynolds number, a dimensionless quantity defined as

$$\mathrm{Re} = \frac{\rho v L}{\eta}, \tag{1.3}$$

where v is a characteristic velocity scale and L is a characteristic length scale of the flow. The Reynolds number can be interpreted as the ratio of inertial forces (scaling as $\rho v^2/L$) to viscous forces (scaling as $\eta v/L^2$).

For macroscopic flows familiar from everyday experience, water flowing from a tap, air around a moving car, the Reynolds number is typically large ($\mathrm{Re} \gtrsim 10^3$), and inertial effects dominate. Turbulence, vortex shedding, and momentum-driven phenomena characterize this regime. In stark contrast, microscopic swimmers operate at Reynolds numbers many orders of magnitude smaller. As famously calculated in the landmark paper "Life at Low Reynolds Number" by Purcell [17], a bacterium swimming at 30 μm/s has $\mathrm{Re} \approx 10^{-5}$, while a human sperm cell achieves $\mathrm{Re} \approx 10^{-2}$. Even the largest single-celled organisms rarely exceed $\mathrm{Re} \sim 1$.

At such low Reynolds numbers, viscous dissipation overwhelms any tendency for inertial coasting. A microorganism that stops swimming comes to rest almost instantaneously, within a distance comparable to the size of an atom. This complete absence of inertia

fundamentally changes the character of locomotion and necessitates strategies qualitatively different from those employed by macroscopic swimmers.

1.2.3. The Stokes Equations and Low Reynolds Number Flow

When $\mathrm{Re} \ll 1$, the nonlinear inertial terms in the Navier-Stokes equations become negligible compared to the viscous terms. Dropping these terms yields the Stokes equations (also known as the creeping flow equations):

$$\nabla p = \eta \nabla^2 \mathbf{v} + \mathbf{f}, \tag{1.4}$$

together with the incompressibility condition $\nabla \cdot \mathbf{v} = 0$. The Stokes equations are linear in the velocity field, which has profound consequences for the physics of low Reynolds number flows.

Three key properties distinguish Stokes flow from high Reynolds number hydrodynamics, as discussed, for example, in "Low Reynolds Number Hydrodynamics" by Happel and Brenner [18]:

Linearity: The velocity field depends linearly on the applied forces and boundary conditions. If two different forcing configurations produce velocity fields $\mathbf{v}_1$ and $\mathbf{v}_2$, their superposition produces $\mathbf{v}_1 + \mathbf{v}_2$. This linearity enables powerful analytical techniques and simplifies the analysis of complex geometries.

Instantaneity: The Stokes equations contain no time derivatives of velocity, the flow responds instantaneously to changes in boundary conditions or forcing. There is no memory of previous flow states, and the velocity field at any instant depends only on the current configuration of boundaries and forces.

Time-reversibility: If a sequence of boundary motions produces a particular fluid flow, then reversing the sequence in time produces exactly the reversed flow. This property, which follows from the linearity and instantaneity of the Stokes equations, has dramatic consequences for locomotion at low Reynolds numbers.

1.2.4. The Scallop Theorem

The time-reversibility of Stokes flow imposes a fundamental constraint on swimming at low Reynolds numbers, elegantly articulated by Purcell in "Life at Low Reynolds Number" [17] through what has become known as the *scallop theorem*.

Consider a swimmer that changes its shape through a sequence of configurations and then returns to its original shape by reversing that sequence exactly. Such motion is called *reciprocal* because the forward and backward strokes are related by time reversal. The scallop theorem states that reciprocal motion produces zero net displacement in Stokes flow.

The proof follows directly from time-reversibility. During the forward stroke, the swimmer moves through the fluid by some displacement $\Delta\mathbf{r}$. During the backward stroke, which retraces the same sequence of shapes in reverse, the fluid flow is exactly reversed, and the swimmer returns to its starting position with displacement $-\Delta\mathbf{r}$. The net displacement over one complete cycle is therefore zero.

The theorem takes its name from the scallop, which swims by opening and closing its shell, a motion with only one degree of freedom that is necessarily reciprocal. At high Reynolds numbers, a scallop achieves net displacement because the rapid closing stroke generates more thrust than the slow opening stroke (due to the quadratic dependence of drag on velocity in the inertial regime). But a microscopic scallop, operating at $\mathrm{Re} \ll 1$, would make no progress regardless of how it varied the speed of opening and closing.

The scallop theorem establishes that microswimmers must employ *non-reciprocal* motions, stroke sequences that cannot be mapped onto their time-reversed counterparts. Breaking the symmetry between forward and backward strokes is the essential requirement for locomotion in the viscous-dominated regime.

1.2.5. Non-Reciprocal Locomotion Strategies

Microorganisms have evolved diverse strategies to overcome the constraints imposed by the scallop theorem. A comprehensive review of these locomotion mechanisms is provided, for example, in "The Hydrodynamics of Swimming Microorganisms" by Lauga and Powers [19].

Flagellar propulsion: Many bacteria, such as *Escherichia coli*, swim by rotating helical flagella [8], [9]. The chirality of the helix breaks time-reversal symmetry: clockwise and counterclockwise rotation produce different flow patterns, enabling propulsion. Eukaryotic cells like sperm use a different mechanism, their flagella execute planar or helical bending waves that propagate along the filament [7], achieving non-reciprocal motion through the traveling wave character of the deformation.

Ciliary beating: Ciliates such as *Paramecium* are covered with hundreds of short hair-like appendages called cilia. Each cilium executes an asymmetric beat cycle: a stiff "power stroke" that sweeps through the fluid, followed by a curved "recovery stroke" close to the cell surface [11]. The geometric difference between these strokes renders the motion non-reciprocal and generates net propulsion.

Body deformation: Some organisms swim through coordinated deformation of their entire body rather than relying on specialized appendages. Amoeboid cells can generate traveling waves of surface deformation [6], while certain algae achieve locomotion through shape changes of their cell body. This mode of swimming is particularly relevant for cells lacking flagella or cilia and represents the biological motivation for the present work.

Surface slip velocity: An alternative theoretical framework describes swimming in terms of a prescribed tangential velocity at the swimmer's surface, without specifying the underlying mechanism that generates this velocity. This approach, embodied in the squirmer model discussed below, provides a unified description of surface-driven locomotion.

1.3. Theoretical Models for Microswimmers

1.3.1. The Squirmer Model

The squirmer model, introduced by Lighthill in "On the Squirming Motion of Nearly Spherical Deformable Bodies through Liquids at Very Small Reynolds Numbers" [20] and extended by Blake in "A Spherical Envelope Approach to Ciliary Propulsion" [21], provides a canonical theoretical framework for analyzing microswimmer hydrodynamics.

In this model, the swimmer is represented as a sphere with a prescribed tangential surface velocity. The surface velocity is expanded in terms of Legendre polynomials:

$$v_\theta(\theta) = \sum_{n=1}^{\infty} B_n V_n(\cos\theta), \tag{1.5}$$

where θ is the polar angle measured from the swimming direction, B_n are amplitude coefficients, and V_n are related to derivatives of Legendre polynomials. The first two modes have particularly clear physical interpretations: B_1 determines the swimming velocity, while B_2 characterizes the far-field flow generated by the swimmer.

The ratio $\beta = B_2/B_1$ classifies squirmers into three categories:

- **Pushers** ($\beta < 0$): Generate thrust from behind, like bacteria with rear-mounted flagella. The far-field flow is extensile along the swimming axis.
- **Pullers** ($\beta > 0$): Generate thrust from the front, like the algae *Chlamydomonas*. The far-field flow is contractile along the swimming axis.
- **Neutral swimmers** ($\beta = 0$): Generate no force dipole, producing a faster-decaying far-field flow.

The squirmer model has proven enormously useful for studying hydrodynamic interactions, collective behavior, and swimming near boundaries. However, it treats the swimmer as a rigid body with kinematically prescribed surface motion, neglecting the mechanical compliance of real biological membranes and the coupling between surface deformation and fluid forces.

1.3.2. Geometric Phases and Shape Space

A deeper theoretical understanding of non-reciprocal locomotion emerged from the work of Shapere and Wilczek in the late 1980s, particularly in "Geometry of Self-Propulsion at Low Reynolds Number" [22] and "Self-Propulsion at Low Reynolds Number" [23].

These authors recognized that swimming at low Reynolds numbers can be understood in terms of *geometric phases*, a concept borrowed from quantum mechanics and gauge theory. The key insight is that the configuration space of a deformable swimmer can be decomposed into "shape space" (describing the internal degrees of freedom) and "position space" (describing location and orientation).

A cyclic sequence of shape changes, one that returns the swimmer to its original shape, traces a closed loop in shape space. The net displacement acquired over this cycle depends

only on the geometry of this loop, not on how quickly it is traversed. Non-reciprocal strokes correspond to loops that enclose nonzero area in shape space, while reciprocal strokes trace paths that retrace themselves and enclose zero area.

This geometric framework provides powerful tools for optimizing swimming strokes and understanding the relationship between shape changes and locomotion. It also makes clear why at least two independent shape degrees of freedom are required for swimming: with only one degree of freedom, any closed loop in shape space necessarily retraces itself and is therefore reciprocal.

1.3.3. The Gap: Deformable Membrane-Bound Cells

Despite the theoretical advances described above, a significant gap remains between idealized models and the reality of biological cell locomotion. Most existing models fall into one of two categories:

Rigid swimmers with prescribed kinematics: The squirmer model and its extensions treat the swimmer body as rigid, with surface velocities specified *a priori* rather than emerging from the mechanics of the system. This approach cannot capture how membrane elasticity, bending rigidity, or internal forces influence swimming performance.

Highly specific biological models: Detailed models of bacterial flagella [15], sperm tails [7], or ciliary arrays [10] faithfully represent particular biological systems but may not generalize to other modes of cell locomotion. These models often require extensive parameterization from experimental data.

The intermediate regime, a generic deformable cell that swims through coordinated surface deformations, remains underexplored. Key questions are unanswered: How do membrane mechanical properties such as bending rigidity affect swimming velocity and efficiency? How does the coupling between surface elasticity and hydrodynamic forces shape the deformation dynamics? Can a simple mechanical model capture the essential physics of deformable cell locomotion?

Addressing these questions requires computational approaches that can simultaneously resolve membrane mechanics and fluid hydrodynamics without prescribing the swimming kinematics in advance.

1.4. Motivation and Objectives of This Work

This thesis develops and analyzes a computational model for deformable cell swimming that bridges the gap between rigid squirmer models and the complexity of real biological cells. The approach couples a triangulated surface model for the cell membrane with Multi-Particle Collision Dynamics (MPCD) for the surrounding fluid, enabling fully resolved hydrodynamic interactions without prescribed swimming kinematics.

The specific objectives of this work are:

1. **Develop a deformable swimmer model:** Implement a triangulated surface representation of a membrane-bound cell with realistic mechanical properties including elasticity, bending rigidity, and volume conservation. Couple this model

to an MPCD fluid that captures the essential physics of low Reynolds number hydrodynamics.

2. **Achieve locomotion through non-reciprocal deformation:** Design a forcing protocol that drives the cell surface through non-reciprocal shape changes, enabling sustained swimming motion. Verify that the swimming mechanism satisfies the constraints imposed by the scallop theorem.

3. **Characterize the swimming dynamics:** Analyze the relationship between surface deformation patterns and swimming velocity. Examine the phase-space structure of the deformation cycle and its connection to propulsion.

4. **Investigate the role of membrane mechanics:** Conduct systematic parameter studies to understand how membrane properties, particularly bending rigidity, influence swimming performance. Identify regimes of efficient locomotion and understand the physical mechanisms underlying parameter-dependent behavior.

5. **Connect to canonical microswimmer theory:** Test whether the deformable swimmer obeys the scaling relationships predicted by theoretical models, particularly the dependence of swimming velocity on deformation amplitude and frequency.

By pursuing these objectives, this work aims to establish how mechanical properties of deformable membranes govern locomotion at low Reynolds numbers, providing insights relevant to both biological cell motility and the design of synthetic microswimmers.

1.5. Thesis Outline

This thesis is organized as follows:

Chapter 2: Simulation Methods. We describe the computational framework underlying our simulations. This includes the triangulated surface model for the deformable cell membrane, the interaction potentials governing surface mechanics, and the Multi-Particle Collision Dynamics algorithm for simulating the surrounding fluid. We also detail the coupling mechanisms between the cell and fluid and define the geometric descriptors used to characterize cell shape.

Chapter 3: Results and Discussion. We present the main findings of our simulation studies. Beginning with the basic swimming behavior and center-of-mass trajectories, we proceed to analyze phase-dependent deformation patterns and their correlation with instantaneous velocity. We examine finite-size effects and establish the canonical velocity-deformation relationship. A comprehensive parameter study investigates how bending rigidity modulates swimming performance and reveals a transition between forward and backward swimming regimes.

Chapter 4: Conclusion and Outlook. We summarize the key findings, discuss their implications for understanding biological cell motility and microswimmer design, and suggest directions for future research.

2. Simulation Methods

2.1. Cell Model

2.1.1. Model Overview

Biological membranes have a thickness much smaller than their overall size, allowing representation as two-dimensional surfaces in three-dimensional space. Therefore we model the surface of a deformable cell as a triangulated surface. Cell nodes are placed on a spherical surface and are connected through triangulation. The interaction potentials between nodes reproduce the mechanical behavior of biological cells and vesicles. The surface mechanics include contributions from the membrane and cytoskeletal components. Different potential strengths can model varying cell mechanical properties.

Surface discretization uses Delaunay triangulation [24]. This method creates triangular meshes from nodes on spherical surfaces while satisfying the Delaunay condition: each triangle's circumcircle contains only its three nodes. The triangular mesh enables force calculations for mechanical properties like bending elasticity.

A triangulation factor of 10 was used, generating 1002 surface nodes with 3000 edges and 2000 triangular faces. Most nodes have six neighbors, with few having five connections. Higher factors give smoother surfaces but increase computational cost. The chosen factor provides good geometric accuracy with reasonable computational requirements. Delaunay triangulation creates a bond length distribution rather than uniform spacing.

The cell's mechanical response is determined by interaction potentials that encode elasticity, bending rigidity, and constraints on volume. To translate these physical properties into a Molecular Dynamics (MD) simulation, analytical force expressions must be derived from each potential energy functional, allowing forces to be computed from particle coordinates. The following sections present each interaction potential, derive the corresponding force expressions, and describe their implementation. All potentials are based on formulations from a prior master's thesis from our research group [25].

The interaction potentials introduce several parameters that govern the cell's mechanical and dynamic behavior. This work systematically investigates how a subset of these parameters affects swimming performance. The key parameters studied fall into two categories: surface properties and driving parameters. For surface properties, we focus on the bending rigidity k_{Bend}, which controls resistance to out-of-plane deformation. The driving parameters characterize the internal deformation mechanism: the triangle force amplitude F_{tfa} and triangle force period T_{tfp}, which together determine the strength and frequency of the non-reciprocal shape changes that propel the cell. By varying these parameters, we can identify regimes of efficient swimming and understand how surface softness or stiffness influences locomotion strategy.

2.1.2. Bond Potential

The bond vector connecting nodes i and j is defined as $\mathbf{r}_{ij} \equiv \mathbf{r}_i - \mathbf{r}_j$, where the bond length is given by $r_{ij} \equiv |\mathbf{r}_{ij}|$. The corresponding unit vector is expressed as $\hat{\mathbf{r}}_{ij} \equiv \frac{\mathbf{r}_{ij}}{r_{ij}}$. Let B represent the collection of all $N_B = 3000$ surface bonds. The harmonic bond potential energy is formulated as:

$$U_{Bond} = \frac{k_{Bond}}{2} \sum_{\langle i,j \rangle} (r_{ij} - r_{ij,0})^2 \tag{2.1}$$

where $\langle i, j \rangle$ denotes summation over all bonded pairs of nodes, k_{Bond} represents the bond stiffness parameter, and $r_{ij,0}$ is the equilibrium bond length, taken from the initial triangulated sphere configuration.

The spatial gradient of the bond length with respect to node i position, where $\nabla_i \equiv \left(\frac{\partial}{\partial x_i}, \frac{\partial}{\partial y_i}, \frac{\partial}{\partial z_i}\right)^T$, can be derived as:

$$\nabla_i r_{ij} = \nabla_i |\mathbf{r}_i - \mathbf{r}_j| = \frac{\mathbf{r}_i - \mathbf{r}_j}{|\mathbf{r}_i - \mathbf{r}_j|} = \frac{\mathbf{r}_{ij}}{r_{ij}} = \hat{\mathbf{r}}_{ij} \tag{2.2}$$

Consider B_i as the set of bonds involving node i. The mechanical force acting on node i at position $\mathbf{r}_i$ is calculated through:

$$\begin{aligned} \mathbf{F}_{Bond,i} &= -\nabla_i U_{Bond} \\ &= -k_{Bond} \sum_{j \in B_i} [(r_{ij} - r_{ij,0}) \nabla_i r_{ij}] \\ &= -k_{Bond} \sum_{j \in B_i} [(r_{ij} - r_{ij,0}) \hat{\mathbf{r}}_{ij}] \end{aligned} \tag{2.3}$$

The net bond force on node i is therefore given by:

$$\mathbf{F}_{Bond,i} = -k_{Bond} \sum_{j \in B_i} [(r_{ij} - r_{ij,0}) \hat{\mathbf{r}}_{ij}] \tag{2.4}$$

When $r_{ij} < r_{ij,0}$, this generates a repulsive force that pushes node i away from node j, whereas $r_{ij} > r_{ij,0}$ produces an attractive force that pulls node i toward node j.

2.1.3. Stillinger-Weber Potential

The Stillinger-Weber (SW) potential prevents bond rupture by providing strong restoring forces when bond lengths deviate significantly from equilibrium. This potential supplements the harmonic bond interactions with attractive and repulsive contributions that activate only at large displacements [26]. While the SW potential was typically not included in previous implementations [25], it proves essential in this work to maintain surface integrity during the pronounced deformations required for swimming locomotion. The interaction generates strong forces to maintain bonds within acceptable length ranges.

Consider a surface bond with vector $\mathbf{r}_{ij}$ and length r_{ij}. The SW potential consists of separate attractive and repulsive components with parameters satisfying $l_{min} < l_{c,1} < l_{c,0} < l_{max}$. Here, k_{SW} denotes the strength of the SW potential, l_{min} and l_{max} define the hard limits beyond which bonds cannot be compressed or stretched, and $l_{c,1}$ and $l_{c,0}$ mark the inner thresholds where the repulsive and attractive contributions begin to activate, respectively. These parameters are chosen such that the SW potential remains inactive under normal thermal fluctuations and harmonic bond dynamics, but provides strong restoring forces when bonds approach critical extension or compression. The specific values used in this work are given in Section 2.4.2.

Attractive potential. For bonds stretched beyond $l_{c,0}$, the attractive potential activates:

$$U_{SW,A} = \begin{cases} k_{SW}\frac{1}{l_{max}-r_{ij}} \exp\left\{\frac{1}{l_{c,0}-r_{ij}}\right\} & \text{for } r_{ij} > l_{c,0} \\ 0 & \text{otherwise} \end{cases} \tag{2.5}$$

The force contribution for $r_{ij} > l_{c,0}$ is:

$$\mathbf{F}_{SW,A,i} = -\frac{k_{SW}}{l_{max}-r_{ij}} \exp\left\{\frac{1}{l_{c,0}-r_{ij}}\right\}\left[\frac{1}{(l_{c,0}-r_{ij})^2} + \frac{1}{l_{max}-r_{ij}}\right]\hat{\mathbf{r}}_{ij} \tag{2.6}$$

Repulsive potential. For compressed bonds below $l_{c,1}$, the repulsive potential activates:

$$U_{SW,R} = \begin{cases} k_{SW}\frac{1}{r_{ij}-l_{min}} \exp\left\{\frac{1}{r_{ij}-l_{c,1}}\right\} & \text{for } r_{ij} < l_{c,1} \\ 0 & \text{otherwise} \end{cases} \tag{2.7}$$

The repulsive force contribution for $r_{ij} < l_{c,1}$ becomes:

$$\mathbf{F}_{SW,R,i} = \frac{k_{SW}}{r_{ij}-l_{min}} \exp\left\{\frac{1}{r_{ij}-l_{c,1}}\right\}\left[\frac{1}{(r_{ij}-l_{c,1})^2} + \frac{1}{r_{ij}-l_{min}}\right]\hat{\mathbf{r}}_{ij} \tag{2.8}$$

The bond length is effectively constrained to $l_{min} < r_{ij} < l_{max}$ while the SW interaction remains inactive in the central range $l_{c,1} < r_{ij} < l_{c,0}$. Parameter selection ensures minimal interference under normal conditions, but strong restoring forces are activated for large deviations.

2.1.4. Bending Potential

The resistance of biological membranes to bending is a crucial mechanical property that determines cell shape and deformation behavior. Following the Helfrich model, the bending energy of a membrane surface is proportional to the squared mean curvature integrated over the surface [27]. The local mean curvature H at a point on the surface is defined as the arithmetic mean of the principal curvatures:

$$H = \frac{1}{2}\left(\frac{1}{R_1} + \frac{1}{R_2}\right), \tag{2.9}$$

where R_1 and R_2 denote the principal radii of curvature. The total bending energy is then given by

$$U_{\text{Bend}} = 2k_{\text{Bend}} \int_S H^2 \, \mathrm{d}A, \tag{2.10}$$

with k_{Bend} being the bending modulus and S the membrane surface. This formulation implies that the energetically favored configuration corresponds to zero mean curvature, i.e., a flat sheet. While a spontaneous curvature H_0 could be incorporated to favor curved equilibrium shapes, this is not employed in the present work. The Gaussian curvature contribution to the Helfrich energy is omitted here, as it remains constant for surfaces of fixed topology and therefore does not contribute to the forces [27].

For the triangulated membrane representation used in this work, the continuous bending energy must be discretized. Guckenberger et al. [28] provide a comprehensive comparison of various discretization schemes for computing bending forces on triangulated surfaces. The approach adopted here corresponds to their "Method B," which employs a discretized form of the Laplace–Beltrami operator Δ_S to evaluate the mean curvature. The Laplace–Beltrami operator generalizes the standard Laplacian to curved manifolds embedded in Euclidean space and provides a robust means of computing surface curvatures from discrete vertex positions.

The discretization yields an analytical expression for the bending force acting on each membrane vertex. Given the positions $\{\mathbf{r}_1, \ldots, \mathbf{r}_N\}$ of all N membrane nodes, the bending force on vertex i is obtained as the negative gradient of the bending energy:

$$\mathbf{F}_{\text{Bend},i} = -\nabla_i U_{\text{Bend}}(\mathbf{r}_1, \ldots, \mathbf{r}_N). \tag{2.11}$$

The explicit form of this force expression involves contributions from neighboring vertices and the local triangulation geometry; the complete derivation and resulting formulas are given in Ref. [28]. This bending interaction acts on all membrane vertices and, together with the other membrane potentials, governs the mechanical response of the cell surface to deformation.

2.1.5. Volume Potential

A harmonic potential maintains constant cell volume by penalizing deviations from the equilibrium volume. The interaction strength is k_V and the equilibrium volume is V_0. The potential is expressed as:

$$U_V = \frac{k_V}{2}(V - V_0)^2 \tag{2.12}$$

The total volume is decomposed into individual tetrahedral contributions from each surface triangle. Let T_i represent all surface triangles, giving $V = \sum_{t \in T_i} V_t$. Using $\nabla_i V = \sum_t \nabla_i V_t$, the force on node i becomes:

$$\mathbf{F}_{V,i} = -\nabla_i U_V = -k_V(V - V_0)\nabla_i V = \sum_t (-k_V)(V - V_0)\nabla_i V_t \equiv \sum_t \mathbf{F}_{V_t,i} \tag{2.13}$$

Consider the force contribution $\mathbf{F}_{V_t,i} = -k_V(V - V_0)\nabla_i V_t$ from the volume element V_t. Each tetrahedral element connects the three surface triangle nodes with the surface center of mass $\mathbf{r}_c$. For surface triangle nodes $\mathbf{r}_i$, $\mathbf{r}_j$, and $\mathbf{r}_k$ connected to $\mathbf{r}_c$, the tetrahedral volume is calculated using the triple product:

$$V_t = \frac{1}{6}|(\mathbf{r}_i - \mathbf{r}_c) \cdot [(\mathbf{r}_j - \mathbf{r}_c) \times (\mathbf{r}_k - \mathbf{r}_c)]| \tag{2.14}$$

The gradient calculation yields:

$$\nabla_i V_t = \frac{1}{6}[(\mathbf{r}_j - \mathbf{r}_c) \times (\mathbf{r}_k - \mathbf{r}_c)] \tag{2.15}$$

Let j_t and k_t denote the nodes that together with node i constitute triangle $t \in T_i$. The total volume force on node i is:

$$\mathbf{F}_{V,i} = \frac{k_V}{6}(V_0 - V) \sum_{t \in T_i} [(\mathbf{r}_{j_t} - \mathbf{r}_c) \times (\mathbf{r}_{k_t} - \mathbf{r}_c)] \tag{2.16}$$

The cross product points roughly in the direction of $\mathbf{r}_i$. For $V < V_0$, the force pushes node i away from the center, increasing surface area and volume. For $V > V_0$, the force pulls node i toward the center, decreasing volume.

2.1.6. Triangle Force Actuation and Driving Mechanism

The active driving mechanism employed in this work is inspired by the three-bead microswimmer model introduced by Rizvi et al. [29]. In their original formulation, three spherical beads are connected by springs in a triangular configuration, with time-dependent oscillatory forces applied along each spring to generate non-reciprocal motion. The triangular design enables autonomous steering capabilities, allowing the microswimmer to follow complex curved paths through coordinated phase-shifted forcing of each spring.

We adapt this concept to our deformable cell model by selecting three membrane nodes that form an equilateral triangle in the equatorial plane of the initial spherical configuration. These three nodes, highlighted in red in Figure 2.1b, serve as the vertices where the active driving forces are applied. The spring-like connections in the original bead-swimmer model correspond to the membrane edges connecting these three nodes, with time-dependent edge lengths L_1, L_2, and L_3. This triangle serves as the fundamental geometric unit controlling the deformation pattern.

The equatorial plane is defined as the horizontal slice through the center of the cell at $z = 30$, where the driving triangle achieves its maximum cross-sectional area. This location is chosen to characterize deformations in a region representative of the bulk cell geometry, away from the poles where the surface curvature is highest. The three edge lengths L_1, L_2, and L_3 form the perimeter of this triangle, and their time-dependent variations represent the deformation of the cell surface during swimming.

The key difference between our implementation and the original three-bead swimmer lies in the mechanical coupling: while the beads in Rizvi's model are connected only to

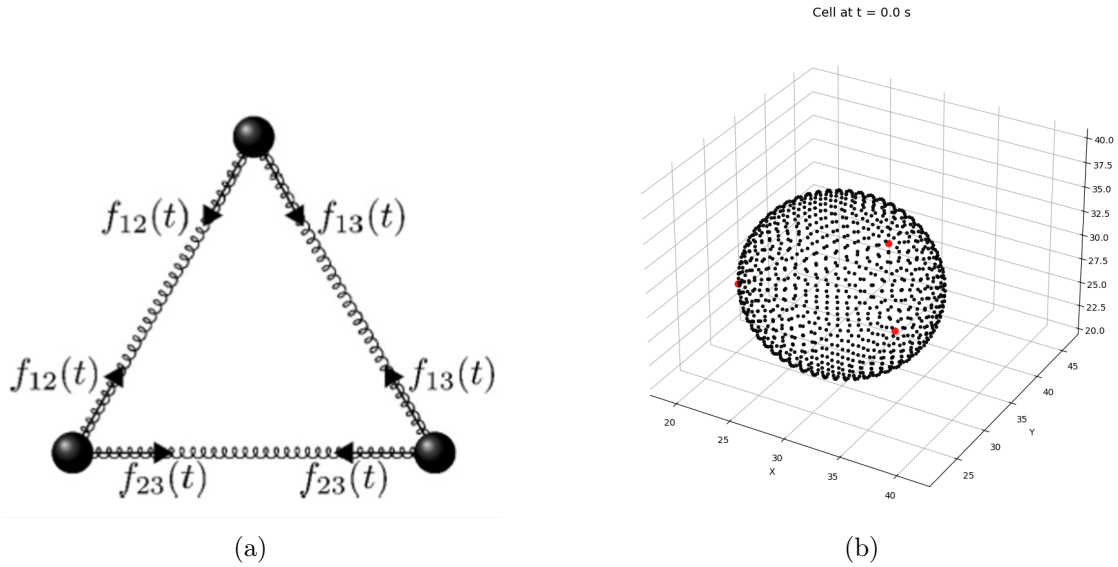

(a) (b)

Figure 2.1.: Adaptation of the three-bead swimmer concept to the deformable cell model. (a) Schematic of the triangular three-bead swimmer from Rizvi et al. [29], showing three beads connected by springs with time-dependent forces $f_{12}(t)$, $f_{13}(t)$, and $f_{23}(t)$ acting along each edge. (b) Initial configuration of our triangulated cell model at $t = 0$, with the three vertices of the driving triangle highlighted in red. These nodes correspond to the three beads in the original model, and the membrane edges connecting them serve as the oscillating "springs" that drive non-reciprocal deformation.

each other through discrete springs, our driving triangle is embedded within a continuous elastic membrane. Consequently, the forces applied at the three vertices propagate through the entire cell surface via the bond, bending, and volume potentials described in Sections 2.1.2–2.1.5. This coupling transforms the localized actuation into global cell deformation, enabling the whole-body shape changes required for swimming.

Force Application Geometry

Each edge length L_α ($\alpha = 1, 2, 3$) experiences a time-dependent force that modulates its value according to a prescribed oscillation pattern. The force magnitude is characterized by the triangle force amplitude F_{tfa}, while the oscillation timescale is set by the triangle force period T_{tfp} [29].

For each node $i \in \{1, 2, 3\}$ of the driving triangle, the force is directed along the connecting edges to neighboring triangle nodes:

$$\mathbf{F}_{\text{drive},i}(t) = F_{\text{tfa}} \left[\hat{\mathbf{e}}_{i,i+1} \sin(\omega t + \alpha_i) - \hat{\mathbf{e}}_{i-1,i} \sin(\omega t + \alpha_{i-1}) \right], \tag{2.17}$$

where $\hat{\mathbf{e}}_{i,j}$ denotes the unit vector pointing from node i to node j, $\omega = 2\pi/T_{\text{tfp}}$ is the angular frequency, and α_i are phase offsets that control the temporal sequence of edge

contractions. The indices are understood cyclically, so that node indices wrap around (i.e., node 4 refers to node 1). The time-dependent forces $f_{12}(t)$, $f_{13}(t)$, and $f_{23}(t)$ shown in Figure 2.1a correspond to these edge-directed forces, with the phase relationships between edges determining whether the resulting motion is reciprocal or non-reciprocal.

Phase Relationships

The phase offsets are chosen to create a specific deformation sequence that breaks time-reversal symmetry [29]:

$$\alpha_1 = 0, \tag{2.18}$$

$$\alpha_2 = \frac{\pi}{2}. \tag{2.19}$$

The phase difference $\Delta\alpha = \pi/2$ corresponds to a quarter-period delay between successive edge contractions. This temporal offset ensures that the cell passes through different shape configurations during the first and second halves of each period, constituting the non-reciprocal motion required by the scallop theorem for net displacement at low Reynolds numbers.

The implementation includes runtime verification that the total driving force vanishes ($\sum_i \mathbf{F}_{\text{drive},i} = \mathbf{0}$), ensuring force-free swimming conditions where locomotion arises purely from shape changes rather than external forcing.

Symmetry Considerations

The geometric arrangement of the driving triangle possesses a two-fold symmetry: edge lengths L_1 and L_2 are related by reflection across the axis defined by L_3. Edge lengths L_1 and L_2 oscillate in phase with each other due to the force geometry, maintaining this mirror symmetry instantaneously at each moment during the deformation cycle. However, the phase-shifted forcing of L_3 breaks the three-fold rotational symmetry of the equilateral triangle, creating an asymmetric deformation sequence over time.

Resulting Deformation Modes

Under this forcing protocol, the driving triangle undergoes periodic shape changes characterized by:

- Synchronized elongation and contraction of L_1 and L_2, maintaining the reflection symmetry about the L_3 axis;
- Phase-shifted oscillation of L_3 with larger amplitude than L_1 and L_2;
- A closed trajectory in the (L_1, L_2, L_3) phase space representing the limit cycle of steady-state swimming.

The amplitude of deformation is controlled by F_{tfa}, with larger values producing greater edge length variations and correspondingly larger swimming velocities. The period T_{tfp} sets the stroke frequency $f = 1/T_{\text{tfp}}$, which together with the deformation amplitude determines the swimming velocity according to the canonical scaling relationship discussed in Chapter 3.

2.1.7. Geometric and Shape Descriptors

To quantify the geometric deformation of the cell surface during swimming, we employ several shape parameters derived from the gyration tensor and the instantaneous node positions.

Center of Mass

The center of mass (COM) of the cell is computed as the arithmetic mean of all surface node positions:

$$\mathbf{r}_c = \frac{1}{N_{\text{nodes}}} \sum_{i=1}^{N_{\text{nodes}}} \mathbf{r}_i, \tag{2.20}$$

where $\mathbf{r}_i$ denotes the position of node i. The COM position is recorded at each timestep and serves as the primary observable for characterizing swimming motion.

Gyration Tensor and Asphericity

The gyration tensor $\mathbf{G}$ characterizes the spatial distribution of the cell surface nodes. It is computed from the node positions $\mathbf{r}_i$ relative to the center of mass $\mathbf{r}_c$:

$$G_{\alpha\beta} = \frac{1}{N_{\text{nodes}}} \sum_{i=1}^{N_{\text{nodes}}} (r_{i,\alpha} - r_{c,\alpha})(r_{i,\beta} - r_{c,\beta}), \tag{2.21}$$

where $\alpha, \beta \in \{x, y, z\}$ denote Cartesian components.

Diagonalization of $\mathbf{G}$ yields three eigenvalues $\lambda_1^2 \leq \lambda_2^2 \leq \lambda_3^2$, sorted in ascending order. These eigenvalues correspond to the squared principal radii of gyration along the principal axes of the cell's shape, with λ_3^2 representing the direction of greatest spatial extent.

The squared radius of gyration is given by the trace of the gyration tensor:

$$R_g^2 = \lambda_1^2 + \lambda_2^2 + \lambda_3^2. \tag{2.22}$$

The asphericity parameter b quantifies the deviation of the cell shape from a perfect sphere:

$$b = \frac{3}{2}\lambda_3^2 - \frac{R_g^2}{2} = \lambda_3^2 - \frac{1}{2}\left(\lambda_1^2 + \lambda_2^2\right). \tag{2.23}$$

For a perfectly spherical shape, all three eigenvalues are equal and $b = 0$. Any deviation from spherical symmetry results in $b > 0$, with larger values indicating more pronounced elongation along the principal axis of greatest extent.

The acylindricity c measures the deviation from cylindrical symmetry:

$$c = \lambda_2^2 - \lambda_1^2, \tag{2.24}$$

which vanishes when the two smaller eigenvalues are equal, indicating rotational symmetry about the principal axis.

Deformation Amplitude

The deformation amplitude ε_2 provides a time-averaged measure of the surface displacement from its equilibrium spherical configuration:

$$\varepsilon_2 = \frac{1}{N_{\text{nodes}} N_T} \sum_{i=1}^{N_T} \sum_{j=1}^{N_{\text{nodes}}} \left| |\mathbf{r}_j(t_i) - \mathbf{r}_c(t_i)| - R_0 \right|, \tag{2.25}$$

where $\mathbf{r}_j(t_i)$ is the position of node j at time t_i, $\mathbf{r}_c(t_i)$ is the center of mass position, R_0 is the equilibrium radius, and N_T is the number of time steps over which the average is computed. For an undeformed sphere, $\varepsilon_2 = 0$, while any deformation yields $\varepsilon_2 > 0$.

2.2. Multiparticle Collision Dynamics

Multi-Particle Collision Dynamics (MPCD), introduced by Malevanets and Kapral [30], [31], offers an efficient approach to simulate hydrodynamic interactions in soft matter systems by explicitly representing fluid degrees of freedom through discrete particles. Rather than solving the Navier-Stokes equations on a fixed mesh, MPCD treats the fluid as an ensemble of point particles that interact through stochastic collisions, naturally producing thermal fluctuations required for accurate low Reynolds number physics. This particle-based formulation is particularly well-suited for systems where immersed structures deform or move dynamically, as it avoids the geometric constraints of grid-based methods [32], [33].

2.2.1. Simulation of the Fluid

The MPCD fluid consists of N_p point particles, each with position $\mathbf{r}_i$, velocity $\mathbf{v}_i$, and mass m_f, maintained at temperature T. At initialization, particles are distributed uniformly throughout the simulation domain with velocities sampled from a Gaussian distribution with characteristic speed $\sqrt{k_B T/m_f}$, where k_B denotes the Boltzmann constant. Throughout this work, all quantities are expressed in dimensionless simulation units [34]: lengths in units of a_0, masses in units of m_f, and energies in units of $k_B T$, with $a_0 = m_f = k_B T = 1$. Velocities are measured in units of $\sqrt{k_B T/m_f}$ and times in units of $a_0\sqrt{m_f/k_B T}$. The system evolves through a repeating cycle of two operations: the streaming phase, during which particles propagate ballistically, followed by a local collision phase in which momentum is redistributed among particles in spatial cells.

During the streaming phase, particles move ballistically according to

$$\mathbf{r}_i(t + \Delta t_{\mathrm{MPCD}}) = \mathbf{r}_i(t) + \mathbf{v}_i(t)\Delta t_{\mathrm{MPCD}}, \tag{2.26}$$

where the time increment $\Delta t_{\mathrm{MPCD}} = 0.01$ (in simulation units) controls both the particle mean free path and the effective fluid viscosity. After streaming, the domain is partitioned into cubic collision cells of side length a_0. Within each cell, all particles undergo a velocity redistribution designed to conserve cell-level momentum. The updated velocities take the form

$$\mathbf{v}_i(t + \Delta t_{\mathrm{MPCD}}) = \mathbf{u}_\alpha(t) + R_\alpha\left[\mathbf{v}_i(t), \mathbf{u}_\alpha(t)\right], \tag{2.27}$$

where $\mathbf{u}_\alpha(t)$ is the center-of-mass velocity of collision cell α and R_α represents a stochastic collision operator applied uniformly to all particles within the cell. In this work, we employ the Andersen thermostat as the collision operator [35], which both preserves total momentum and permits kinetic energy fluctuations. The stochasticity inherent in this collision step generates thermal motion without explicit noise injection.

Figure 2.2 illustrates these two fundamental steps of the MPCD algorithm. The streaming phase (Figure 2.2a) shows particles moving ballistically through the domain, while the collision phase (Figure 2.2b) depicts the partitioning of particles into cubic cells where momentum redistribution occurs.

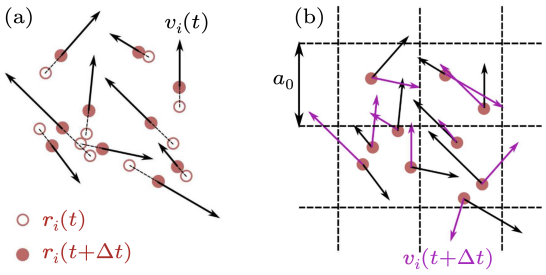

Figure 2.2.: 2D illustration of the MPCD technique (from Ref. [36]). (a) During the streaming phase, fluid particles propagate ballistically. (b) During the collision phase, fluid particles are partitioned into cubic cells and redistribute momentum among all particles within each cell while conserving the local total momentum.

2.2.2. Coupling of Microswimmers to the Fluid

In hybrid MPCD-MD simulations coupling immersed objects to the MPCD fluid, the immersed objects typically evolve on shorter timescales than the fluid. While fluid particles change positions and velocities in relatively large steps Δt_{MPCD}, immersed objects update their positions and conformations at smaller Molecular Dynamics timesteps Δt_{MD} to resolve the relevant molecular scales. This multi-scale approach requires careful treatment of the momentum transfer between the fluid and immersed objects. Large solid objects such as cell bodies are typically treated as impenetrable to fluid particles. Momentum and angular momentum exchange between the object and the MPCD fluid occurs in the streaming step. When a fluid particle collides with the object boundary, it is effectively reflected using the bounce-back rule [37], [38], and the local momentum transfer is applied to the object. See Section 2.3 for our implementation.

To improve statistical properties and reduce unphysical correlations, the collision cell grid is shifted by a random displacement at each time step, independently in each spatial direction. This random shift ensures that particle assignments to cells change from one timestep to the next, restoring Galilean invariance.

2.2.3. Periodic Boundary Conditions

To simulate bulk fluid behavior while maintaining a computationally manageable number of particles, periodic boundary conditions are employed. The simulation domain is replicated infinitely in all spatial directions, creating a space-filling array of identical copies of the original box [39].

When a particle exits the simulation box through one boundary, it is replaced by an image particle entering from the opposite side. Denoting the position of particle i as $\mathbf{r}_i = (x_i, y_i, z_i)$, the coordinates of the departing particle are mapped back into the

primary box by adding or subtracting the box length L along the relevant coordinate:

$$x_i \to x_i - L \quad \text{if} \quad x_i \geq L, \tag{2.28}$$

$$x_i \to x_i + L \quad \text{if} \quad x_i < 0, \tag{2.29}$$

with analogous expressions for y_i and z_i. This wrapping procedure is applied after each integration step [40].

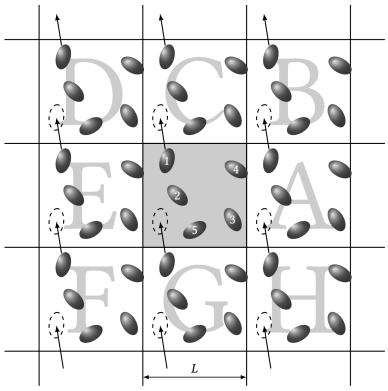

Figure 2.3.: Illustration of periodic boundary conditions in two dimensions. The central simulation box (highlighted region) is replicated in all directions. Particles exiting one boundary reenter from the opposite side. This illustration is taken from Ref. [40].

2.2.4. Regime of Operation: Low Reynolds Number Swimming

The Reynolds number, introduced in Section 1.2.2, can be computed directly from the simulation parameters to verify that our model operates in the appropriate physical regime.

The fluid density in MPCD is determined by the particle number density, which is the number of fluid particles per unit volume. In our three-dimensional cubic collision cells of side length a_0, defined in Section 2.2.1, the density is given by

$$\rho = \frac{N_f}{a_0^3} = 10 \text{ particles per collision cell.} \tag{2.30}$$

The characteristic swimming velocity of the cell is measured from the center-of-mass displacement over one oscillation period:

$$v_c \approx \frac{\Delta x}{T} = 0.1 \text{ (in simulation units).} \tag{2.31}$$

The characteristic length scale is taken as the diameter of the cell, $D = 2R_0 = 16.5\, a_0$. The dynamic viscosity of the MPCD fluid emerges from the collision procedure and is given by [41]

$$\eta \approx \frac{9}{12\Delta t_{\text{MPCD}}} \approx 75 \text{ (in simulation units).} \tag{2.32}$$

With these parameters, the Reynolds number for the swimming cell is

$$\mathrm{Re} = \frac{v_c D \rho}{\eta} \approx 0.22. \tag{2.33}$$

This confirms that our simulations operate in the low Reynolds number regime where viscous forces dominate and inertial effects are negligible.

2.3. Cell-Fluid Coupling

The simulation of deformable membranes immersed in a solvent using MPCD requires accurate coupling mechanisms to mediate momentum and energy exchange between the cell structure and the coarse-grained fluid particles [37], [41]. Two primary mechanisms facilitate this coupling: the bounce-back rule during the streaming step and momentum exchange during the collision step [37], [38].

2.3.1. Streaming Step Momentum Exchange: The Bounce-Back Rule

The principal mechanism governing the interaction between the cell surface and the solvent particles occurs during the MPCD streaming step. During this phase, fluid particles move ballistically according to Equation (2.26), and the cell surface acts as an impermeable boundary.

Collision detection proceeds in two stages. First, the algorithm determines whether a fluid particle has crossed the infinite plane defined by a triangular surface element by examining whether the sign of the scalar product between the particle's displacement vector and the triangle's outward normal has changed between consecutive timesteps. Second, the algorithm verifies whether the particle trajectory actually intersects the triangular region itself using Cramer's rule. Only when both conditions are satisfied is the bounce-back rule applied.

When a collision is detected between fluid particle i and triangle j, momentum is exchanged according to the Noguchi-Gompper approach [37]. The velocity of the fluid particle after collision is given by

$$\mathbf{v}_i' = \mathbf{v}_i - \frac{2m_{\text{tri}}}{m_f + m_{\text{tri}}} \left(\mathbf{v}_i - \mathbf{v}_\triangle\right), \tag{2.34}$$

where $m_{\text{tri}} = 3m_c$ is the effective mass of the triangle (the sum of masses of its three constituent nodes), m_f is the mass of the fluid particle, and $\mathbf{v}_\triangle$ is the mean velocity of the three triangle vertices. The fluid particle position is reset to its pre-collision location to enforce impermeability. Simultaneously, the triangle velocity is updated to

$$\mathbf{v}_\triangle' = \mathbf{v}_\triangle + \frac{2m_f}{m_f + m_{\text{tri}}} \left(\mathbf{v}_i - \mathbf{v}_\triangle\right), \tag{2.35}$$

ensuring momentum conservation. The velocity change is distributed equally to all three nodes comprising the triangle.

Throughout each MPCD timestep, the cumulative momentum change from all particle-surface collisions is tracked and verified to satisfy $\sum_{\text{collisions}}(\Delta\mathbf{p}_{\text{fluid}} + \Delta\mathbf{p}_{\text{surface}}) = 0$ to within machine precision.

2.3.2. Collision Step Momentum Exchange

As a additional coupling mechanism, momentum exchange also occurs during the MPCD collision step. This coupling is achieved by treating cell surface nodes as full participants in the standard MPCD collision procedure.

Cell Nodes as Collision Particles

Each cell node is assigned a position, velocity, and mass $m_c = 10\, m_f$, and participates equally with fluid particles in the collision cell dynamics. When the simulation domain is partitioned into cubic collision cells, both fluid particles and cell nodes are assigned to cells based on their instantaneous positions.

Center-of-Mass Velocity and Collision Dynamics

During the collision step, the center-of-mass velocity $\mathbf{u}_\alpha$ within each collision cell α is computed by averaging the velocities of all particles present:

$$\mathbf{u}_\alpha = \frac{m_f \sum_{i\in\alpha} \mathbf{v}_i^{\text{fluid}} + m_c \sum_{j\in\alpha} \mathbf{v}_j^{\text{cell}}}{m_f N_{\text{fluid},\alpha} + m_c N_{\text{cell},\alpha}}, \tag{2.36}$$

where $N_{\text{fluid},\alpha}$ and $N_{\text{cell},\alpha}$ are the counts of fluid particles and cell nodes in cell α. The collision procedure redistributes velocities using the Andersen thermostat [42]:

$$\mathbf{v}_i^{\text{new}} = \mathbf{v}_{\text{random},i} + \mathbf{u}_\alpha - \mathbf{v}_{\text{E},\alpha}, \tag{2.37}$$

where $\mathbf{v}_{\text{random},i}$ is drawn from a Gaussian distribution with zero mean and standard deviation $\sqrt{k_B T_0/m_f}$ for fluid particles or $\sqrt{k_B T_0/m_c}$ for cell nodes, and $\mathbf{v}_{\text{E},\alpha}$ is the mass-weighted average of random velocities in the cell. This rule is applied identically to both fluid particles and cell nodes.

Momentum Conservation

The collision step enforces momentum conservation at two scales. Local conservation within each cell requires

$$\sum_{i\in\alpha}^{\text{fluid}} m_f \mathbf{v}_i^{\text{old}} + \sum_{j\in\alpha}^{\text{cell}} m_c \mathbf{v}_j^{\text{old}} = \sum_{i\in\alpha}^{\text{fluid}} m_f \mathbf{v}_i^{\text{new}} + \sum_{j\in\alpha}^{\text{cell}} m_c \mathbf{v}_j^{\text{new}}. \tag{2.38}$$

Global conservation across the entire system is also verified at each timestep.

Together, the bounce-back rule and collision step coupling establish bidirectional, multi-scale hydrodynamic coupling between the deformable surface and the surrounding fluid.

2.4. Implementation and Analysis Methods

2.4.1. Computational Implementation

The simulation framework is implemented in Fortran 90, chosen for its computational efficiency in numerically intensive calculations. The codebase builds upon established MPCD implementations developed within our research group [25], with extensions developed specifically for this work to enable deformable cell swimming with triangle-based forcing.

External Libraries and Routines

The implementation relies on several external libraries:

- **Surface triangulation**: The initial spherical mesh is generated using icosahedral subdivision via the `sphere_gridpoints_icos2` routine. Delaunay triangulation on the sphere is performed using the STRIPACK library [43], specifically the `trmesh` routine for constructing the triangulation data structure and `trlist` for converting to triangle adjacency lists.
- **Random number generation**: Thermal fluctuations in the MPCD collision step require efficient generation of Gaussian-distributed random numbers, accomplished using the Ziggurat algorithm [44].
- **Linear algebra**: Eigenvalue decomposition of the gyration tensor for shape characterization is performed using the `DSYEV` routine from LAPACK [45].

Novel Implementations

Several components were developed specifically for this work (see also Appendix A for specific implementation details):

Triangle Force Driving Mechanism. The swimming mechanism described in Section 2.1.6 is implemented in the `tr_compr_force` subroutine. The implementation includes runtime verification that the total force vanishes, ensuring force-free swimming conditions.

Pole Compression Force. An alternative axisymmetric driving mode is implemented in the `compression_force` subroutine, applying oscillating forces between the two pole nodes:

$$\mathbf{F}_{\text{pole}}(t) = \pm F_{\text{cf}}\, \hat{\mathbf{e}}_{12} \cos(\omega t), \tag{2.39}$$

where $\hat{\mathbf{e}}_{12}$ is the unit vector pointing from the north pole to the south pole, and the opposite signs ensure zero net force. This mode produces axisymmetric prolate-oblate oscillations but generates no net swimming due to reciprocal kinematics, serving as a validation case for the non-reciprocal triangle forcing.

Fluid-Membrane Coupling. The bounce-back collision rule described in Section 2.3.1 is implemented in the `particles_check` subroutine. Triangle-particle intersections are detected using a spatial partitioning scheme that tracks which triangles are within reach of each fluid particle.

Shape Analysis Routines. Cell shape characterization is performed through eigenvalue decomposition of the gyration tensor, with built-in validation tests verifying that computed eigenvalues satisfy the characteristic equation.

Molecular Dynamics Integration Scheme

The membrane nodes evolve according to the velocity Verlet algorithm, a symplectic integrator providing second-order accuracy while preserving phase space structure [46], [47].

The integration proceeds in two stages. In the first half-step, velocities are updated using current forces, followed by a position update:

$$\mathbf{v}_i\left(t+\tfrac{\Delta t_{\mathrm{MD}}}{2}\right) = \mathbf{v}_i(t) + \frac{\Delta t_{\mathrm{MD}}}{2m_c}\mathbf{F}_i(t), \tag{2.40}$$

$$\mathbf{r}_i(t+\Delta t_{\mathrm{MD}}) = \mathbf{r}_i(t) + \Delta t_{\mathrm{MD}}\,\mathbf{v}_i\left(t+\tfrac{\Delta t_{\mathrm{MD}}}{2}\right), \tag{2.41}$$

where $\mathbf{F}_i(t)$ is the total force on node i:

$$\mathbf{F}_i = \mathbf{F}_{\mathrm{bond},i} + \mathbf{F}_{\mathrm{bend},i} + \mathbf{F}_{V,i} + \mathbf{F}_{\mathrm{SW},i} + \mathbf{F}_{\mathrm{drive},i}. \tag{2.42}$$

After updating positions, forces are recomputed and velocities complete their update:

$$\mathbf{v}_i(t+\Delta t_{\mathrm{MD}}) = \mathbf{v}_i\left(t+\tfrac{\Delta t_{\mathrm{MD}}}{2}\right) + \frac{\Delta t_{\mathrm{MD}}}{2m_c}\mathbf{F}_i(t+\Delta t_{\mathrm{MD}}). \tag{2.43}$$

2.4.2. Simulation Protocol

All quantities in this section are given in the dimensionless units defined in Section 2.2.1.

Timestep Hierarchy

The hybrid MD-MPCD simulation employs a hierarchical timestep structure:

- MD integration timestep: $\Delta t_{\mathrm{MD}} = 0.001$
- MPCD collision timestep: $\Delta t_{\mathrm{MPCD}} = 0.01$

This ratio of 10 MD steps per MPCD step ensures membrane deformations are well-resolved while maintaining computational efficiency. Within each MPCD timestep, the simulation executes:

1. **Membrane evolution**: 10 MD integration steps using velocity Verlet

2. **Fluid streaming**: Ballistic update of fluid particle positions
3. **Bounce-back collisions**: Momentum exchange at fluid-membrane intersections
4. **MPCD collision step**: Stochastic velocity redistribution within collision cells

For a typical driving period of $T_{\text{tfp}} = 100$, one complete swimming cycle corresponds to 10,000 MPCD timesteps. Standard production runs span 10^5 MPCD timesteps, yielding 10 complete deformation periods. The first period is discarded as transient, with analysis performed on periods 2–10.

Simulation Domain

The simulation box has dimensions $60 \times 60 \times 60$ in units of the collision cell size a_0, with periodic boundary conditions in all directions. The MPCD fluid contains 10 particles per collision cell on average (see Equation 2.30), corresponding to 2.16×10^6 fluid particles.

Parameter Space

Simulations were performed across the following parameter ranges:

Triangle Force Parameters.

- Amplitude: $F_{\text{tfa}} \in \{100, 200, 400, 800, 1200\}$
- Period: $T_{\text{tfp}} \in \{100, 125, 166.67, 200, 333.33, 500\}$

Membrane Rigidity.

$$k_{\text{Bend}} \in \{100, 200, 300, 500, 1000, 1500, 2000, 2500, 5000, 10000\} \tag{2.44}$$

Other membrane parameters were held constant: $k_{\text{Bond}} = 10$, $k_V = 10$, $k_{\text{SW}} = 80$.

Ensemble Statistics. For each parameter combination, 48 independent runs were performed with different random seeds. Error estimates represent standard deviations across the ensemble.

Computational Resources. Each production run requires approximately 60 hours on a single core of the VSC-4 cluster.

2.4.3. Data Analysis Procedures

Simulation Output

Each run generates time series recorded at every MPCD timestep:

- `evo_properties_membrane.dat`: Energy components, surface area, volume, and COM coordinates

- `evo_trcompr_distances_membrane.dat`: Triangle edge lengths $L_1(t)$, $L_2(t)$, $L_3(t)$
- `evo_quantities_membrane.dat`: Shape descriptors (R_g, asphericity, acylindricity)
- `ini_parameters.dat`: Complete parameter record

Post-Processing

Analysis is performed using Python 3 with NumPy and Matplotlib [48], [49]:

Steady-State Velocity. The mean swimming velocity is computed from COM displacement over steady-state:

$$\langle v_y \rangle = \frac{y_c(t_{\text{end}}) - y_c(t_1)}{t_{\text{end}} - t_1}, \tag{2.45}$$

where $t_1 = T_{\text{tfp}}$ marks the end of the transient period.

Deformation Amplitude. For each edge length $L_i(t)$, the amplitude is:

$$\Delta L_i = \max_{t>t_1} L_i(t) - \min_{t>t_1} L_i(t). \tag{2.46}$$

Canonical Scaling Analysis. Quadratic fits test the relationship $v \propto \varepsilon^2 \omega$, with goodness of fit quantified by:

$$R^2 = 1 - \frac{\sum_i (v_i - \hat{v}_i)^2}{\sum_i (v_i - \bar{v})^2}. \tag{2.47}$$

Ensemble Averaging. Results from 48 runs are combined, with means displayed as solid curves and ± 1 standard deviation as shaded regions.

3. Results and Discussion

This chapter presents and analyzes the swimming behavior of deformable cells in a viscous fluid, simulated using the coupled MD-MPCD framework described in Chapter 2. All quantities are reported in the dimensionless units defined in Section 2.2.1. Our investigation addresses the fundamental mechanisms underlying non-reciprocal cell locomotion at low Reynolds numbers, examining how the geometric and material properties of the cell surface govern swimming performance and deformation dynamics.

Prior to investigating triangle-based swimming locomotion, we conducted preliminary simulations using a simpler deformation mode: periodic compression along the north-south axis of the cell (pole-to-pole forcing). These exploratory runs served to establish suitable parameter ranges for the surface potentials, identify the maximum tolerable force amplitude, and determine appropriate forcing periods for stable periodic deformation. The insights gained from this preliminary study informed the parameter choices used throughout the main investigation, although the pole-to-pole compression mode itself does not produce net swimming due to its reciprocal (time-reversible) character. The results presented in this chapter focus exclusively on the triangle-based forcing mechanism, which breaks time-reversal symmetry and enables sustained locomotion.

We begin by characterizing the swimming motion through center-of-mass trajectories and velocity analysis, establishing the baseline hydrodynamic behavior of the system. Subsequently, we examine phase-dependent deformation patterns and investigate the role of simulation parameters such as box size on swimming velocity. We then analyze the relationship between discrete geometric features of the triangulated surface model specifically the force amplitude and deformation period and the resulting swimming efficiency. The canonical relationships derived from microswimmer theory are compared against our simulation results.

Finally, we conduct a comprehensive parametric study of surface bending rigidity k_{Bend}, exploring how this critical mechanical parameter modulates cell deformation, shape evolution, and swimming velocity across a range of values. Throughout this analysis, we quantify deformation characteristics using the asphericity parameter and the shape factor and deformation amplitude ε_2, while systematically documenting differences between forward and backward swimming modes.

3.1. Center-of-Mass Motion and Swimming Velocity Characterization

3.1.1. Temporal Evolution of Cellular Position

The fundamental measure of swimming success is the net displacement of the cell's center of mass (COM) over time. Figure 3.1 displays the COM trajectories in three spatial dimensions during sustained swimming simulations over approximately 10 deformation cycles. Each deformation cycle corresponds to one complete period of the triangle forcing, $T_{\text{tfp}} = 100$, so the total simulation duration shown is 1000.

The simulations were performed with the following parameters: bending rigidity $k_{\text{Bend}} = 300$, triangle force amplitude $F_{\text{tfa}} = 800$, triangle force period $T_{\text{tfp}} = 100$, and cubic simulation box with edge length $L = 60$. The cell is initialized as an equilibrium sphere with its center of mass located at $(x, y, z) = (30, 30, 30)$, corresponding to the center of the simulation domain. The figure presents comparisons between forward swimming (red curves) and backward swimming (blue curves) motions, with shaded regions indicating the standard deviation across an ensemble of 48 independent simulation runs.

Forward and backward swimming are distinguished by the temporal character of the applied forcing. For forward swimming, the triangle forces follow the protocol described in Section 2.1.6, with edge lengths modulated according to Equation (2.17). Backward swimming is achieved by time-reversing the forcing: the substitution $t \to -t$ in the sinusoidal force functions reverses the temporal sequence of shape changes. This time reversal does not simply negate the swimming velocity; rather, it produces a qualitatively different deformation sequence that propels the cell in the opposite direction (negative y).

The cell swims preferentially along the y-direction due to the symmetry of the forcing geometry. As described in Section 2.1.6, edge lengths L_1 and L_2 oscillate in phase with each other, maintaining mirror symmetry about the axis defined by L_3. This mirror symmetry ensures that any fluid displacements generated in the x-direction by one side of the cell are canceled by equal and opposite displacements from the other side. Similarly, the forcing pattern possesses symmetry with respect to the z-direction, preventing net motion along this axis. Only the y-direction, which coincides with the symmetry axis of the (L_1, L_2) pair, permits net displacement through the coordinated, non-reciprocal deformation of the triangular cross-section apart from noise.

Our simulations reveal an asymmetry in translational motion across spatial dimensions. In both the x and z directions, we observe minimal net displacement. The COM position in these directions remains essentially confined, with fluctuations that are consistent with thermal noise and the symmetry of the forcing geometry. This confinement confirms that the cell swimming mechanism generates primarily one-dimensional motion along the y-axis, as expected from the symmetry considerations discussed above.

In contrast, the y-direction motion displays robust and consistent displacement. The oscillatory features visible in the trajectories correspond to individual deformation cycles: during each period T_{tfp}, the cell executes one complete stroke sequence, producing alternating phases of positive and negative instantaneous velocity. For forward swimming

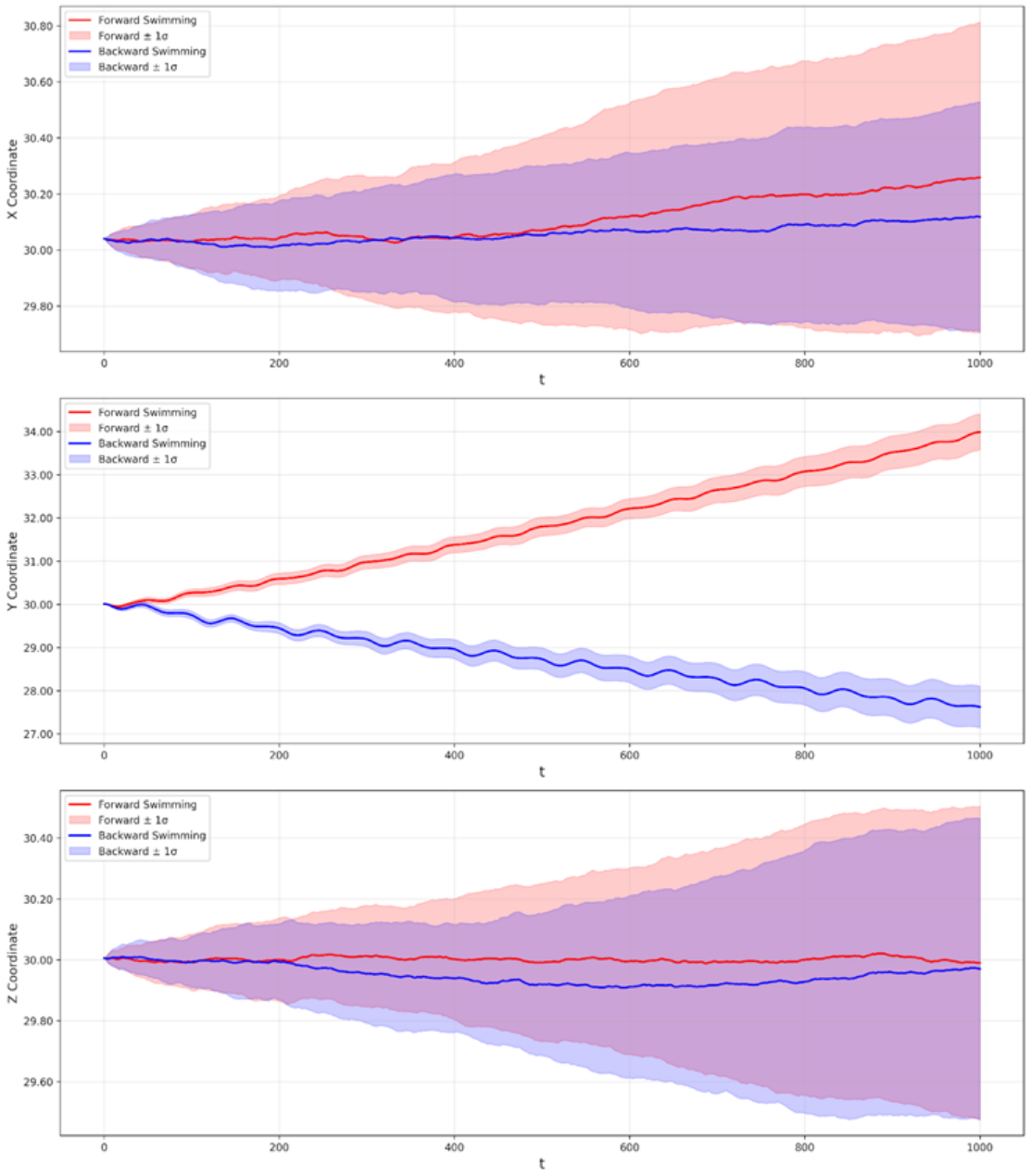

Figure 3.1.: Center of mass trajectories for forward (red) and backward (blue) swimming over 10 complete deformation cycles ($T_{\text{tfp}} = 100$ per cycle, total duration 1000). Top: x-coordinate; Middle: y-coordinate; Bottom: z-coordinate. Shaded regions represent standard deviation across an ensemble of 48 independent simulations. Simulation parameters: $k_{\text{Bend}} = 300$, $F_{\text{tfa}} = 800$, box edge length $L = 60$. Initial COM position: $(30, 30, 30)$.

(red), the positive velocity phases dominate, yielding net displacement in the $+y$ direction. For backward swimming (blue), the negative velocity phases dominate due to the time-reversed forcing, yielding net displacement in the $-y$ direction.

The forward swimming condition exhibits a net displacement from $y = 30$ to $y \approx 34$, representing a net progression of approximately 4 over the simulation duration. The backward swimming condition conversely shows a net displacement from $y = 30$ to $y \approx 27.7$, corresponding to a net displacement of approximately -2.3. Notably, the magnitudes of forward and backward displacements are not equal: $|\Delta y_{\text{forward}}| \approx 4$ exceeds $|\Delta y_{\text{backward}}| \approx 2.3$. This asymmetry is a direct consequence of the viscoelastic properties of the system and will be discussed in detail in Section 3.1.3.

3.1.2. Instantaneous Velocity Oscillations Within Swimming Cycles

A more nuanced picture of swimming dynamics emerges when examining the instantaneous y-direction velocity, v_y (middle panel of Figure 3.1). Rather than exhibiting sustained constant velocity, the cell experiences periodic oscillations in its swimming velocity that are phase-locked to the surface deformation cycle. This oscillatory behavior reflects the non-reciprocal nature of the forcing mechanism: the cell does not maintain uniform motion but instead undergoes alternating periods of acceleration and deceleration that correspond to different phases of the cyclic surface motion.

For the forward swimming case, while the mean velocity over a complete cycle remains positive, the instantaneous velocity shows substantial modulations. During certain phases of the deformation cycle, v_y approaches zero or even becomes slightly negative, as evidenced by dips in the red curve. This behavior, where forward-swimming cells experience periodic negative velocity components, is not a sign of simulation instability but rather reflects the fundamental mechanics of microswimmer locomotion. Such "one-step-back, two-steps-forward" motion is also observed in swimming algae cells [50]: the net forward progress arises from the specific temporal ordering of asymmetric strokes, where the cell advances more during its effective power stroke than it retreats during the recovery phase. Although the cell occasionally moves backward, the asymmetry between these phases produces sustained net propulsion.

Similarly, the backward swimming condition (blue curve) demonstrates oscillations around its mean negative velocity. Periods occur where v_y briefly becomes positive or approaches zero, creating a complex oscillatory pattern superimposed on the net backward drift. The velocity envelope narrows slightly over the course of the simulation as the system approaches true steady-state conditions, with the amplitude of oscillations remaining roughly constant at approximately ± 1 unit around the mean velocity value.

3.1.3. Symmetry Breaking and Viscoelastic Effects

A critical observation emerges from comparing the forward and backward swimming displacements: the magnitudes are not equal. One might naively expect that reversing the force direction would produce a perfectly symmetric response, yielding equal and opposite displacements. However, our results clearly demonstrate that $|\Delta y_{\text{forward}}| \approx 4$ is

larger than $|\Delta y_{\text{backward}}| \approx 2.3$. This asymmetry provides direct evidence that our system does not obey simple time-reversal symmetry.

It is important to clarify the mechanism by which backward motion is generated in our simulations. Rather than implementing true time-reversal which would involve running the simulation backward and inverting all velocities, we achieve backward motion by reversing the sign of the applied forces at each triangular element while maintaining the forward temporal direction of the simulation. This procedure preserves the inherent viscoelastic properties of both the surface and the surrounding fluid, which distinguish forward and backward processes.

The viscoelasticity of the system provides a physical explanation for the observed asymmetry. During the stroke, the surface deforms with a specific velocity profile determined by the interplay between the applied forces, surface elasticity, and viscous drag from the fluid. When forces are reversed (to produce backward motion), the surface finds itself driven in the opposite direction, but its elastic response and the velocity-dependent drag forces are fundamentally asymmetric processes. A viscoelastic medium cannot be perfectly time-reversed by merely reversing external forces the intrinsic damping mechanisms operate with the same dissipative character regardless of motion direction, but the coupling between elastic restoring forces and viscous dissipation creates a nonreciprocal response.

This result is consistent with fundamental principles of non-equilibrium physics and microswimmer theory, which establish that sustained locomotion at low Reynolds numbers requires symmetry breaking. The viscoelastic character of our system provides precisely such a symmetry-breaking mechanism, enabling directional swimming even in the absence of active biochemical processes or complex metabolic regulation. The magnitude difference between forward and backward swimming thus provides valuable insight into the viscous and elastic parameters governing the system dynamics.

3.1.4. Summary of Key Observations

From this initial characterization, several important features of the swimming system emerge: (1) swimming motion is quasi-one-dimensional, confined primarily to a single spatial coordinate despite three-dimensional geometry; (2) instantaneous velocity contains substantial oscillatory components phase-locked to the deformation cycle, even as net displacement is unidirectional; (3) forward and backward swimming modes exhibit asymmetric responses to force reversal, a signature of viscoelastic breaking of time-reversal symmetry. These findings establish the foundation for subsequent analysis of how systematic variation of surface and force parameters modulates these swimming characteristics.

3.2. Shape Dynamics During Swimming

To visualize the periodic shape changes that drive cell locomotion, we present snapshots of the deforming cell over one complete swimming cycle in Figure 3.2. The sequence shows ten configurations captured at intervals of $\Delta t = 10$ time units, spanning a total period of $T = 100$ time units corresponding to one full cycle of the applied triangle forces.

The red markers indicate the triangle vertices where the periodic forces are applied, while the remaining mesh points deform in response to both the applied forces and the internal surface mechanics. The snapshots illustrate how the cell undergoes pronounced shape changes throughout the swimming cycle, transitioning between elongated and compressed configurations. This non-reciprocal sequence of deformations breaks time-reversal symmetry and generates net propulsion in the viscous fluid environment, consistent with the requirements imposed by the Scallop theorem discussed in Subsection 1.2.4.

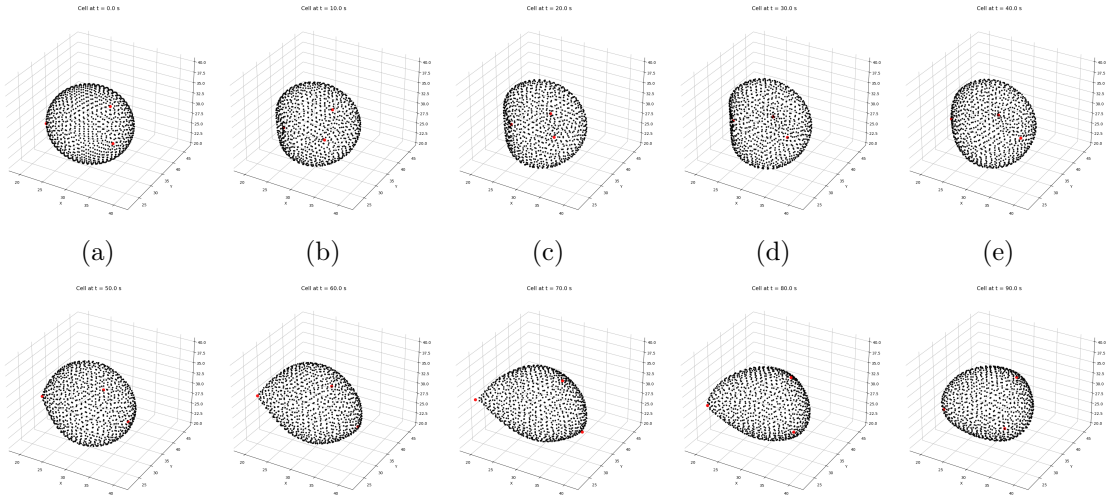

Figure 3.2.: Snapshots of the swimming cell over one complete cycle ($T = 100$ time units). Each panel shows the cell configuration at intervals of $\Delta t = 10$ time units. Red markers indicate the triangle vertices where periodic forces are applied. The sequence demonstrates the characteristic shape deformations that generate swimming motion through non-reciprocal body changes.

3.3. Effects of Simulation Box Size on Swimming Velocity

3.3.1. Motivation and Methodology

A critical concern in molecular dynamics and hydrodynamic simulations with periodic boundary conditions is the potential for finite-size effects to influence the measured physical quantities. The presence of boundaries and periodic boundary conditions can introduce artifacts in the measurement of swimming velocity if the simulation domain is too small relative to the characteristic length scale of the problem. To investigate whether our results are affected by such finite-size effects, we performed a convergence study examining the steady-state swimming velocity across three different cubic simulation box sizes.

3.3.2. Convergence Analysis: Box Size Dependence

The cell in our simulations has a characteristic size of approximately $d_{\text{cell}} \approx 16.5$ length units. We selected simulation box edge lengths such that the computational domain provides sufficient clearance around the swimming cell: specifically, we maintained $\approx 4d_{\text{cell}} \sim 60$ as our reference box edge length for the primary simulations. To verify the adequacy of this choice, we performed steady-state velocity measurements at three box sizes: 40, 50, and 60 units.

Figure 3.3 presents the steady-state velocity as a function of box edge length. The results demonstrate remarkable stability across the tested range. The maximum measured mean velocity is $\langle v_y \rangle_{\max} = 3.88$, while the minimum is $\langle v_y \rangle_{\min} = 3.72$, yielding a relative variation of approximately 4%. This small variation is well within acceptable tolerances for convergence and indicates that even the smallest tested box size (40 units, corresponding to approximately $2.4d_{\text{cell}}$) does not introduce significant finite-size effects that would systematically suppress or enhance the swimming velocity.

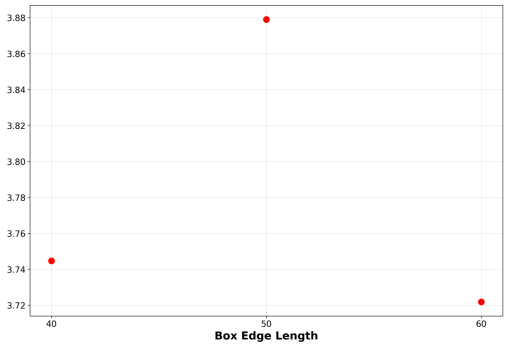

Figure 3.3.: Steady-state swimming velocity $\langle v_y \rangle$ as a function of simulation box edge length. Three simulations were performed at box sizes of 40, 50, and 60 length units. The velocity remains essentially constant, with variation less than 4% across the full range, indicating that finite-size effects are negligible for the swimming velocity measurement.

The apparent scatter in the data (with the intermediate box size yielding slightly higher velocity) may reflect minor differences in the detailed trajectory due to slightly different initial conditions or sampling noise from the finite averaging window, but the overall trend clearly demonstrates convergence. The weak dependence on box size suggests that the periodic boundary conditions do not significantly constrain the cell motion, and that the domain is sufficiently large relative to the hydrodynamic length scale of the problem.

3.3.3. Implications for Subsequent Simulations

Based on this convergence study, we conclude that finite-size effects are not a significant source of error in our velocity measurements. All subsequent simulations reported in this work employ a box edge length of 60 units, which provides a comfortable safety margin while maintaining computational efficiency. The numerical value of the steady-state velocity should therefore be interpreted as representing the intrinsic swimming performance of the deformable cell model, rather than being artificially suppressed or enhanced by confinement effects.

3.4. Phase-Dependent Deformation and Coupling to Instantaneous Swimming Velocity

3.4.1. Geometric-Velocity Coupling

The relationship between surface geometry and locomotion can be established by monitoring the three characteristic edge lengths L_1, L_2, and L_3 (defined in Section 2.1.6 and illustrated schematically in the inset of Figure 2.1a) alongside the instantaneous swimming velocity throughout the deformation cycle. By examining how these geometric descriptors evolve in time and correlate with velocity variations, we can directly connect the phase-dependent shape changes to the resulting propulsion.

3.4.2. Temporal Correlation Between Deformation and Velocity

Figure 3.4 displays the time evolution of the three edge lengths L_1, L_2, L_3 (left axis) and the instantaneous y-direction velocity v_y (right axis) over a 1000 time units simulation spanning approximately 10 complete swimming cycles. The most striking feature of this plot is the pronounced phase locking between the deformation modes and the swimming velocity the velocity oscillations are not random fluctuations but rather directly follow the cell's geometric changes.

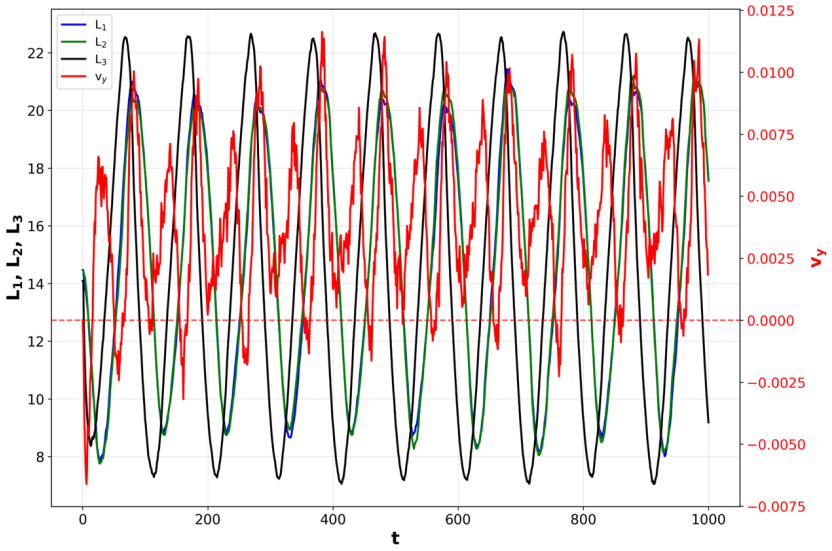

Figure 3.4.: Time evolution of edge lengths L_1, L_2, L_3 and instantaneous swimming velocity v_y over 10 swimming cycles (1000 time units). The three edge lengths represent the deformation of the equilateral triangle geometry of the cell. The left axis shows edge lengths (MPCD units), while the right axis shows velocity v_y (length units per timestep). The clear phase locking between deformation and velocity demonstrates the hydrodynamic coupling between cell shape dynamics and locomotion.

3.4.3. In-Phase Deformation and Symmetry Breaking

A critical observation emerges from examining the relative phases of L_1 and L_2: these two edge lengths oscillate in phase with each other (Figure 3.4). This synchronized behavior is a direct consequence of the force actuation geometry described in Section 2.1.6.

The in-phase oscillation of L_1 and L_2, combined with the phase-shifted response of L_3, breaks the mirror symmetry of the triangular cross-section. This asymmetry is essential for generating net displacement: symmetric expansion and contraction of all three edges would preserve the triangular shape throughout the cycle, producing only reciprocal motion forbidden by the scallop theorem. Instead, the distinct temporal behavior of L_3 relative to L_1 and L_2 creates the non-reciprocal deformation sequence required for low Reynolds number locomotion.

3.4.4. Asymmetric Deformation: The Role of L_3

The deformation amplitude of L_3 is notably larger than those of L_1 and L_2, as is evident from the figure. Moreover, the phase of L_3 relative to L_1 and L_2 is shifted. This asymmetry in deformation both in amplitude and phase is the source of the non-reciprocal motion that enables swimming. The cell does not simply pulse symmetrically; rather, it undergoes a carefully orchestrated sequence of shape changes where different regions of the surface deform at different times and with different magnitudes.

This orchestration is crucial. The transient period at the beginning of the simulation (from $t = 0$ to approximately $t = 100$) shows noticeable irregularities in the deformation pattern, with L_3 initially displaying larger fluctuations in phase and amplitude relative to L_1 and L_2. However, after this initial transient, the deformation pattern stabilizes into a repeating cycle where the phase relationships and amplitude ratios become consistent from cycle to cycle.

3.4.5. Direct Correlation of Deformation Phases with Instantaneous Velocity

The instantaneous swimming velocity v_y (shown in red) exhibits pronounced oscillations that are phase-locked to the deformation cycle. Each peak in v_y corresponds closely to a specific phase of the surface deformation, indicating that certain configurations of the cell geometry are more effective at generating forward propulsion than others. Notably, v_y does not remain constantly positive; rather, it oscillates around a positive mean value, with excursions both above and below zero.

3.4.6. Physical Interpretation: Hydrodynamic Coupling and Shape-Dependent Propulsion

The tight coupling between the deformation pattern and instantaneous velocity demonstrates that swimming velocity in our system is fundamentally a consequence of shape dynamics. The cell does not swim by pushing against a substrate or by maintaining a constant body shape while applying spatially heterogeneous forces. Instead, it achieves

locomotion through the precise temporal coordination of surface deformation, which generates reactive hydrodynamic forces that propel the cell preferentially in one direction.

The asymmetry in how L_3 behaves relative to L_1 and L_2 is the key to understanding this coupling. Because different regions of the cell surface deform at different times and with different amplitudes, the fluid loading on the surface varies in a time-dependent manner. This time-dependent variation in surface geometry creates a net time-asymmetric flow pattern around the cell, even though the driving forces themselves repeat periodically.

3.5. Phase Space Analysis: Geometric Representation of Surface Deformation Dynamics

3.5.1. Phase Space Construction and Trajectory Visualization

To gain deeper insight into the underlying deformation dynamics, we construct phase space representations of the triangular surface geometry. Since the cell surface is modeled using a triangulated surface with three fundamental edge lengths L_1, L_2, and L_3, the instantaneous geometric configuration can be represented as a point in a three-dimensional phase space where each coordinate corresponds to one edge length. As the surface deforms during the swimming cycle, this point traces out a trajectory in phase space, and the structure of this trajectory provides information about the stability, periodicity, and symmetry of the deformation mode.

Figure 3.5 presents complementary views of the phase space dynamics. It shows two-dimensional projections onto the coordinate planes: L_1 versus L_2 (top panel), L_2 versus L_3 (bottom left), L_3 versus L_1 (bottom right) and the full three-dimensional phase space trajectory with L_1, L_2, and L_3 plotted along the x, y, and z axes, respectively. The starting point of each trajectory is marked with a green dot, while the endpoint is indicated by a red dot. The colormap from blue/purple (early times) to yellow/green (later times) provides temporal information along the trajectory path.

3.5.2. Convergence to a Stable Limit Cycle

The most prominent feature visible in both phase space representations is the rapid convergence from the initial transient trajectory to a well-defined closed loop. During the first deformation cycle (approximately the first quarter of the total simulation time, corresponding to the blue/purple portion of the trajectory in Figures 3.5a-d), the phase space path spirals outward from the initial condition (green dot) toward a stable limit cycle. This outward spiral reflects the transient dynamics, where the system adjusts from arbitrary initial edge lengths to the stable periodic orbit dictated by the forcing parameters and surface mechanical properties.

After approximately one complete deformation period, the trajectory settles onto a smooth, closed loop that is traced repeatedly throughout the remainder of the simulation. This closed loop is known in dynamical systems theory as a *limit cycle* a periodic orbit in phase space that acts as an attractor for nearby trajectories. The existence of a stable limit cycle confirms that the swimming motion has reached a true periodic steady state: the surface deformation pattern repeats identically from cycle to cycle, with edge lengths returning precisely to their initial values at the end of each period.

The rapid convergence to the limit cycle (within one deformation period) indicates that the attractor is strongly stable. Any small perturbations in the edge lengths due to thermal fluctuations or numerical noise are quickly damped out as the system returns to the stable periodic orbit. This robustness is essential for sustained swimming, as it ensures that the cell maintains a consistent deformation pattern over many cycles despite the stochastic nature of the surrounding fluid.

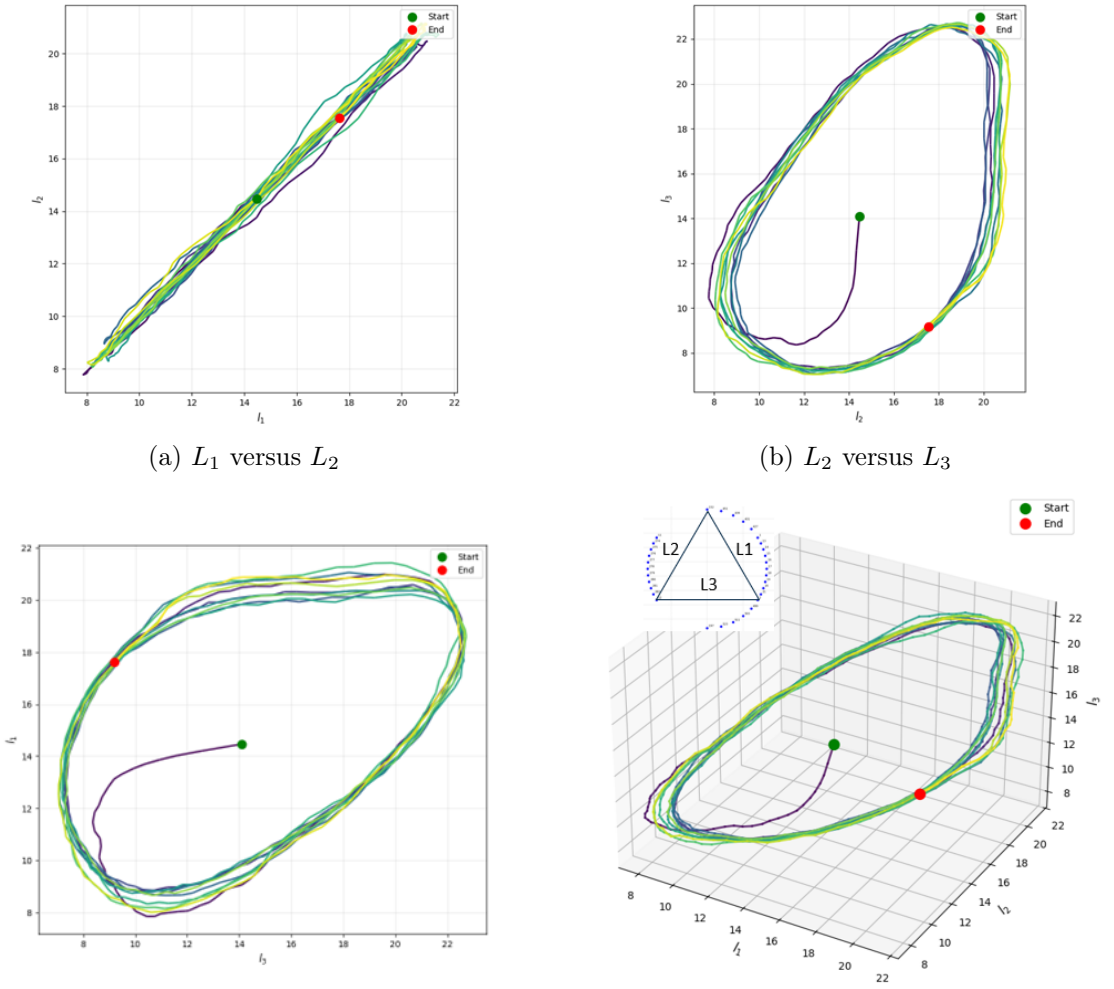

(a) L_1 versus L_2

(b) L_2 versus L_3

(c) L_3 versus L_1

(d) 3D trajectory

Figure 3.5.: Phase space representations of surface deformation dynamics. Panels (a)–(c) show two-dimensional projections onto the coordinate planes, while (d) displays the full three-dimensional trajectory. Green dots mark initial configurations; red dots indicate final states after 10 deformation cycles. The color gradient from blue/purple (early time) to yellow/green (late time) traces temporal evolution. The trajectory rapidly converges to a stable limit cycle. Simulation parameters: $F_{\text{tfa}} = 800$, $T_{\text{tfp}} = 100$, box edge length $= 60$, $k_{\text{Bend}} = 300$.

3.5.3. Implications for Swimming Mechanism and Subsequent Analysis

The existence of a stable, well-defined limit cycle in the deformation phase space has several important implications for understanding the swimming mechanism:

1. **Robust periodic motion:** The limit cycle demonstrates that the cell executes a repeatable, stable swimming stroke that persists over many deformation cycles. This repeatability is essential for sustained locomotion and suggests that the swimming velocity should also stabilize to a well-defined steady-state value (as confirmed in Section 3.3).

2. **Non-reciprocal deformation:** The non-circular, elliptical shape of the limit cycle in the L_2-L_3 and L_3-L_1 planes indicates that the deformation mode is *non-reciprocal*: the sequence of shapes adopted by the cell during one half of the cycle is not the time-reversed sequence of the second half. This non-reciprocity is precisely what enables net displacement at low Reynolds numbers, in accordance with the scallop theorem.

3. **Parameter sensitivity:** The specific geometry of the limit cycle is determined by the simulation parameters (F_{tfa}, T_{tfp}, k_{Bend}). Systematic variation of these parameters will shift the limit cycle in phase space, potentially altering both the deformation amplitude and the phase relationships between edges. Such parametric studies (to be presented in subsequent sections) will reveal how surface mechanics and forcing conditions modulate swimming performance.

4. **Foundation for velocity-deformation correlations:** The stable limit cycle provides a well-defined reference trajectory against which we can compare instantaneous swimming velocity. By tracking the position along the limit cycle and correlating it with the velocity signal, we can identify which phases of the deformation cycle contribute most strongly to forward propulsion an analysis that will be pursued in detail in later sections.

In summary, the phase space analysis confirms that our simulations have successfully achieved a stable, periodic steady-state swimming motion characterized by a robust limit cycle attractor. The geometric structure of this limit cycle encodes the symmetry-breaking deformation pattern that enables locomotion, and its rapid establishment (within one period) validates the convergence of our simulations to physically meaningful steady-state behavior.

3.6. Force-Length Phase Space

To further characterize the mechanical response of the deformable surface to the applied driving forces, we examine the phase space spanned by the instantaneous force and the corresponding edge length of the driving triangle. This force-length representation provides insight into the dynamic force-extension behavior of the surface during cyclic deformation.

Figures 3.6 and 3.7 display the force-length phase portraits for edges L_1 and L_3, respectively, across the full range of force amplitudes ($F_{\text{tfa}} = 200, 400, 800, 1200$) and periods ($T_{\text{tfp}} = 100, 125, 167, 200, 333, 500$). The phase space for L_2 closely resembles that of L_1 due to the symmetry of the forcing protocol and is therefore not shown separately. In each panel, the green marker indicates the beginning of the steady-state regime; the first deformation period is excluded to remove transient behavior.

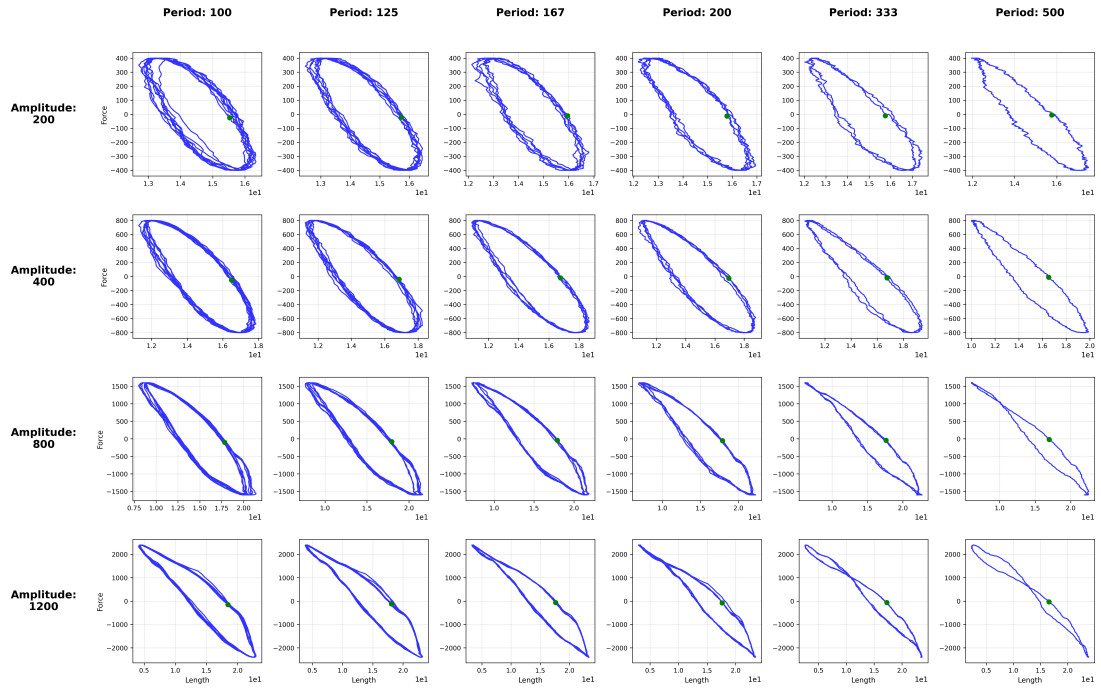

Figure 3.6.: Force-length phase space for edge L_1 across different force amplitudes (rows) and periods (columns). The green marker indicates the onset of steady-state behavior. Higher amplitudes produce cleaner trajectories with reduced noise, while all conditions exhibit a well-defined outer boundary curve characteristic of the surface's mechanical response.

Several features emerge from these phase portraits. First, as the force amplitude increases, the trajectories become progressively smoother with reduced fluctuations. At low amplitudes ($F_{\text{tfa}} = 200$), thermal noise from the MPCD fluid produces visible scatter

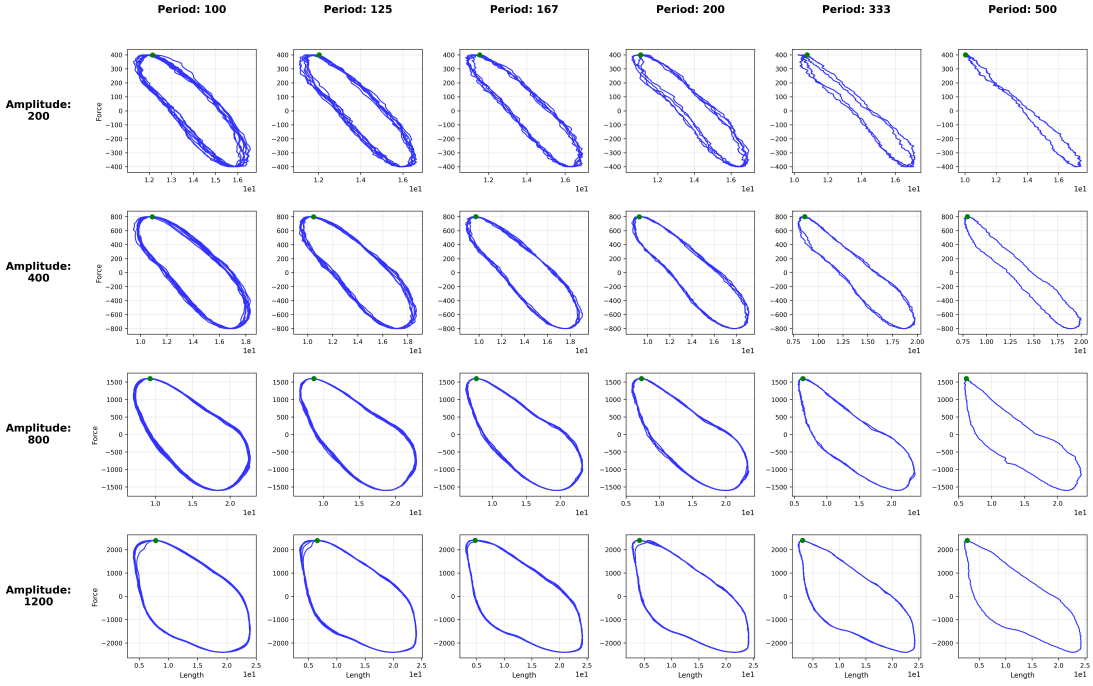

Figure 3.7.: Force-length phase space for edge L_3 across different force amplitudes (rows) and periods (columns). Compared to L_1, the phase portraits show distinctly different shapes, reflecting the different orientation of L_3 relative to the swimming direction and the asymmetric mechanical coupling through the surface.

in the trajectories, while at high amplitudes ($F_{\text{tfa}} = 1200$), the deterministic mechanical response dominates and the curves trace well-defined paths. This trend confirms that the signal-to-noise ratio improves with stronger driving, consistent with the active forces increasingly overwhelming thermal fluctuations.

Second, all trajectories exhibit a clear outer boundary that defines the maximum extent of the phase space accessible under each parameter combination. This boundary reflects the mechanical constraints imposed by the surface potentials: the bond elasticity resists excessive stretching, while the bending and volume potentials limit the overall deformation amplitude. The enclosed area of the phase portrait increases with force amplitude, indicating larger mechanical work performed per cycle.

Third, the phase portraits for L_1 and L_3 show qualitatively different shapes. The L_1 trajectories (and similarly L_2) display relatively symmetric, ellipse-like loops, whereas the L_3 trajectories exhibit more asymmetric, tilted profiles. This difference arises from the geometric relationship between the triangle edges and the swimming direction: L_1 and L_2 are oriented symmetrically with respect to the propulsion axis, while L_3 lies orthogonal to it. The distinct mechanical coupling of L_3 to the global cell deformation produces the

observed asymmetry in its force-length response.

The force-length phase space complements the geometric phase space analysis presented in Section 3.4 by explicitly incorporating the driving forces. Together, these representations provide a comprehensive picture of how the applied actuation translates into surface deformation and ultimately into swimming motion.

3.7. Dependence of Swimming Velocity on Triangle Force Parameters

Having established the basic swimming mechanism, we now investigate how the mean forward-swimming velocity $\langle v_y \rangle$ depends on the two key parameters controlling the internal triangle forcing: the triangle force amplitude F_{tfa} and the triangle force period T_{tfp}.

Figure 3.8 displays the mean swimming velocity as a function of the triangle force period for various triangle force amplitudes. The different colors distinguish the amplitude values ($F_{\text{tfa}} = 100, 200, 400, 800, 1200$), while the marker shapes indicate the period values ($T_{\text{tfp}} = 100, 125, 166.67, 200, 333.33, 500$). A clear decreasing trend is observed: at fixed amplitude, increasing the forcing period leads to reduced swimming velocities. This behavior can be understood from the fact that longer periods correspond to slower deformation cycles, which reduce the rate at which the swimmer generates propulsive strokes. Since swimming at low Reynolds number requires continuous actuation to overcome viscous drag, slower cycling necessarily produces lower time-averaged velocities.

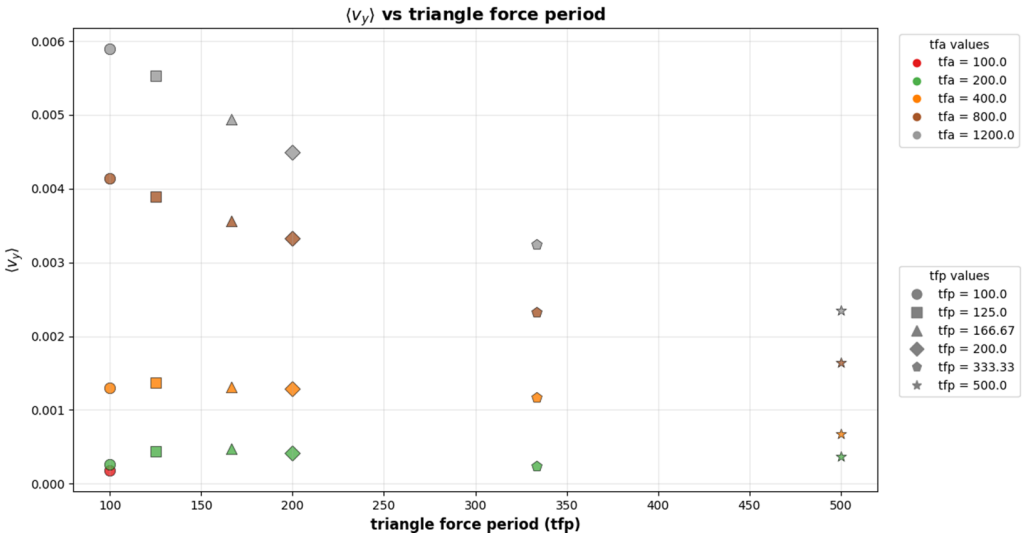

Figure 3.8.: Mean forward-swimming velocity $\langle v_y \rangle$ as a function of triangle force period T_{tfp}. Colors indicate different triangle force amplitudes F_{tfa}, while marker shapes distinguish the period values. The velocity decreases monotonically with increasing period at all amplitudes.

The complementary view is presented in Figure 3.9, which shows the swimming velocity as a function of the triangle force amplitude. Here, the data reveal a monotonically increasing relationship: larger forcing amplitudes produce higher swimming velocities. This trend reflects the fact that stronger internal forces generate larger surface deformations, which in turn displace more fluid per stroke cycle. The resulting enhancement of the non-reciprocal shape changes leads to more effective propulsion. Notably, the velocity appears to scale approximately linearly with amplitude in the intermediate regime, though

deviations from linearity become apparent at the highest amplitudes, suggesting the onset of nonlinear effects in the surface response.

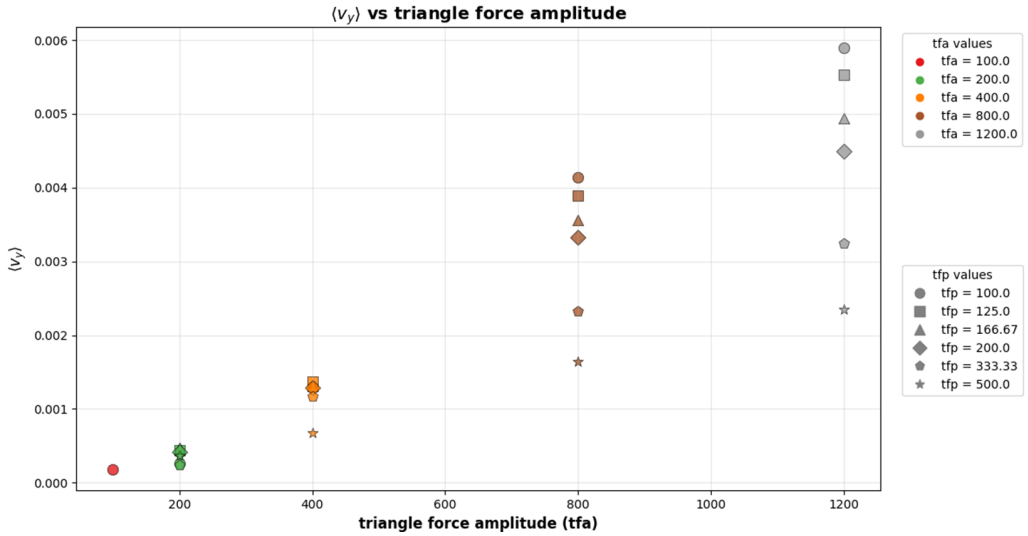

Figure 3.9.: Mean forward-swimming velocity $\langle v_y \rangle$ as a function of triangle force amplitude F_{tfa}. Colors indicate different amplitude values, while marker shapes distinguish the period values. The velocity increases with amplitude, reflecting enhanced propulsion from larger surface deformations.

Together, these results demonstrate that the swimming performance can be tuned through the forcing parameters: higher amplitudes and shorter periods both enhance the swimming velocity. This suggests an optimization strategy for maximizing locomotion efficiency within the constraints imposed by the surface mechanics and fluid viscosity.

3.8. Shape Parameter Analysis

Beyond characterizing the swimming velocity, we quantify the geometric deformation of the cell surface using the shape parameters defined in Section 2.1.7: the asphericity b and the deformation amplitude ε_2.

3.8.1. Deformation Amplitude Dependence on Forcing Parameters

Figure 3.10 presents the deformation amplitude ε_2 as a function of both the triangle force period T_{tfp} (left panel) and the triangle force amplitude F_{tfa} (right panel). As in the previous figures, colors distinguish the amplitude values ($F_{\text{tfa}} = 100, 200, 400, 800, 1200$), while marker shapes indicate the period values ($T_{\text{tfp}} = 100, 125, 166.67, 200, 333.33, 500$).

The left panel reveals that the deformation amplitude increases with the forcing period but eventually plateaus at higher periods. This behavior has a clear physical interpretation: longer periods correspond to slower deformation cycles, which allow more time for the surface to respond to the applied forces and reach larger displacements before the forcing reverses direction. However, once the period becomes sufficiently long, the surface has enough time to approach its maximum deformation within each half-cycle, and further increases in period yield diminishing returns.

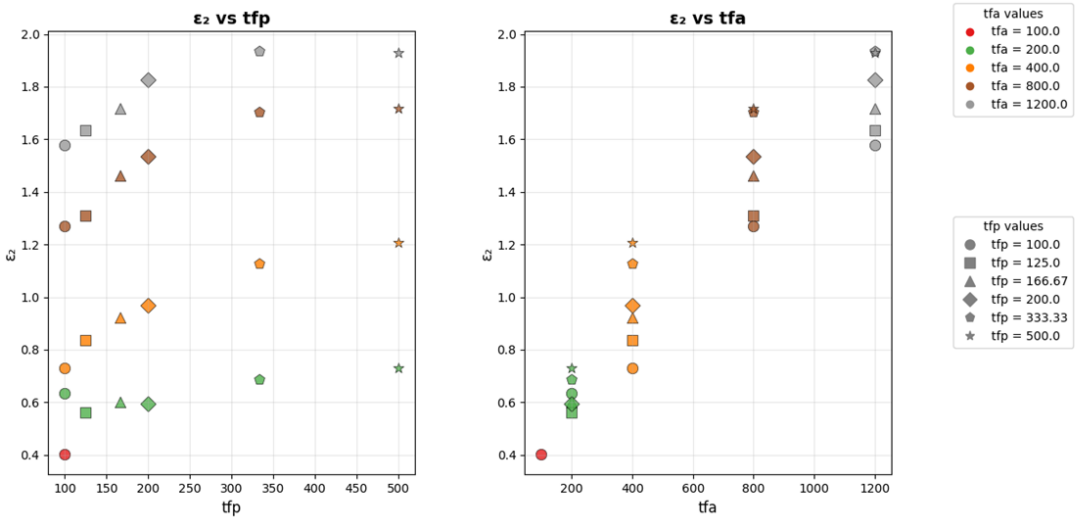

Figure 3.10.: Deformation amplitude ε_2 as a function of triangle force period T_{tfp} (left) and triangle force amplitude F_{tfa} (right). Colors indicate different amplitude values, while marker shapes distinguish the period values. The deformation amplitude increases with period before plateauing, reflecting the surface's finite response time, and increases with amplitude due to stronger forcing.

The right panel demonstrates that the deformation amplitude increases monotonically with the triangle force amplitude. This trend is physically intuitive: stronger internal forces exert larger stresses on the surface, resulting in greater displacements from the

equilibrium configuration. The approximately linear relationship observed at lower amplitudes suggests that the surface response remains within a quasi-linear elastic regime, while the continued increase at higher amplitudes indicates that significant deformations can be achieved without surface failure.

3.9. Canonical Velocity-Deformation Relationship

One of the central results of microswimmer theory is the canonical relationship between swimming velocity, deformation amplitude, and stroke frequency. For small-amplitude swimmers undergoing non-reciprocal shape changes, the mean swimming velocity scales as

$$\langle v_y \rangle \propto \varepsilon_2^2 f \tag{3.1}$$

where ε_2 is the deformation amplitude and $f = 1/T_{\text{tfp}}$ is the forcing frequency. This quadratic dependence on deformation arises from the requirement of non-reciprocal motion [17], [22]: at low Reynolds number, time-reversal symmetry must be broken to achieve net displacement, and the leading-order contribution to swimming velocity emerges at second order in the deformation amplitude.

To test whether our simulations reproduce this fundamental scaling, we plot the mean swimming velocity $\langle v_y \rangle$ against the combined parameter $\varepsilon_2^2 f$ in Figure 3.11. As before, colors distinguish the triangle force amplitude values ($F_{\text{tfa}} = 100, 200, 400, 800, 1200$), while marker shapes indicate the period values ($T_{\text{tfp}} = 100, 125, 166.67, 200, 333.33, 500$).

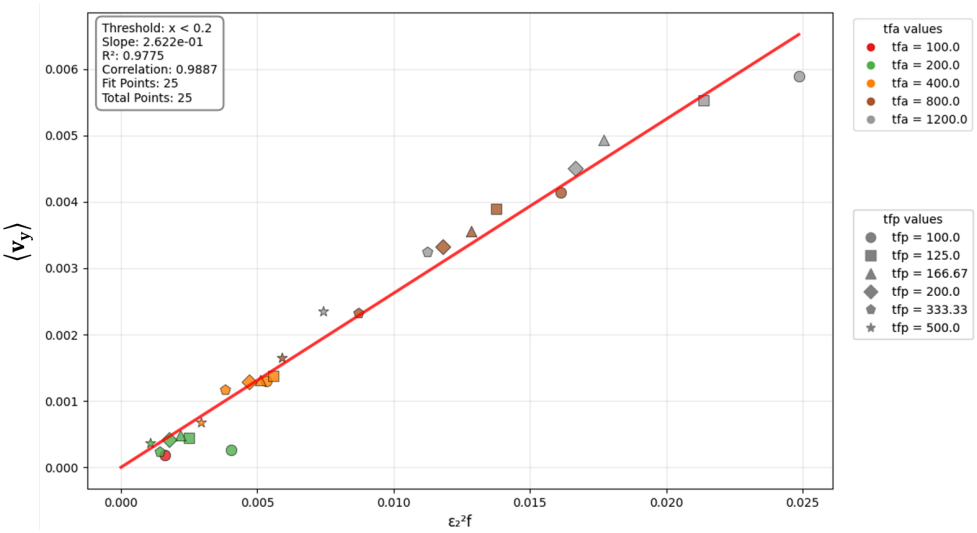

Figure 3.11.: Mean swimming velocity $\langle v_y \rangle$ as a function of the combined parameter $\varepsilon_2^2 f$, demonstrating the canonical microswimmer scaling relationship. The red line represents a linear fit with slope $A = 2.622 \times 10^{-1}$, yielding $R^2 = 0.9775$ and a correlation coefficient of 0.9887. Colors indicate different triangle force amplitudes F_{tfa}, while marker shapes distinguish the period values T_{tfp}. The excellent data collapse confirms that non-reciprocal surface deformation governs the swimming dynamics.

The data collapse onto a single linear trend, confirming the canonical relationship. A linear fit of the form

$$\langle v_y \rangle = A\,\varepsilon_2^2 f \tag{3.2}$$

yields a proportionality constant $A = 2.622 \times 10^{-1}$. The fit quality is excellent, with a correlation coefficient of 0.9887 and a coefficient of determination $R^2 = 0.9775$, indicating that over 97% of the variance in swimming velocity is explained by this simple scaling law. All 25 data points lie close to the fitted line, demonstrating robust agreement across the entire parameter space explored.

This result carries several important implications. First, it validates our computational approach by reproducing a well-established theoretical prediction for microswimmers. Second, the proportionality constant A encapsulates the shape-dependent swimming efficiency of our specific swimmer geometry different surface configurations or internal forcing mechanisms would yield different values of A while preserving the fundamental $\varepsilon_2^2 f$ scaling. Third, the strong correlation confirms that the swimming mechanism in our simulations is driven by non-reciprocal surface deformation, as required by the scallop theorem for locomotion at low Reynolds number.

The observed scaling provides a predictive framework for tuning swimmer performance: to maximize velocity, one should increase either the deformation amplitude (through stronger forcing) or the stroke frequency (through shorter periods), with the deformation amplitude having the dominant effect due to its quadratic contribution.

3.10. Influence of Surface Bending Rigidity on Shape Parameters

The bending rigidity k_{Bend} characterizes the stiffness of the cell surface and its resistance to deformation. To investigate how surface mechanics affect the swimmer's shape during locomotion, we examine the dependence of both the mean asphericity $\langle b \rangle$ and the deformation amplitude ε_2 on the bending rigidity across two orders of magnitude, from $k_{\text{Bend}} = 100$ to $k_{\text{Bend}} = 10000$.

Figure 3.12 presents both shape parameters as functions of the bending rigidity on a logarithmic scale. The mean asphericity $\langle b \rangle$ (blue circles, left axis) and the deformation amplitude ε_2 (red squares, right axis) both exhibit a monotonically decreasing trend with increasing k_{Bend}.

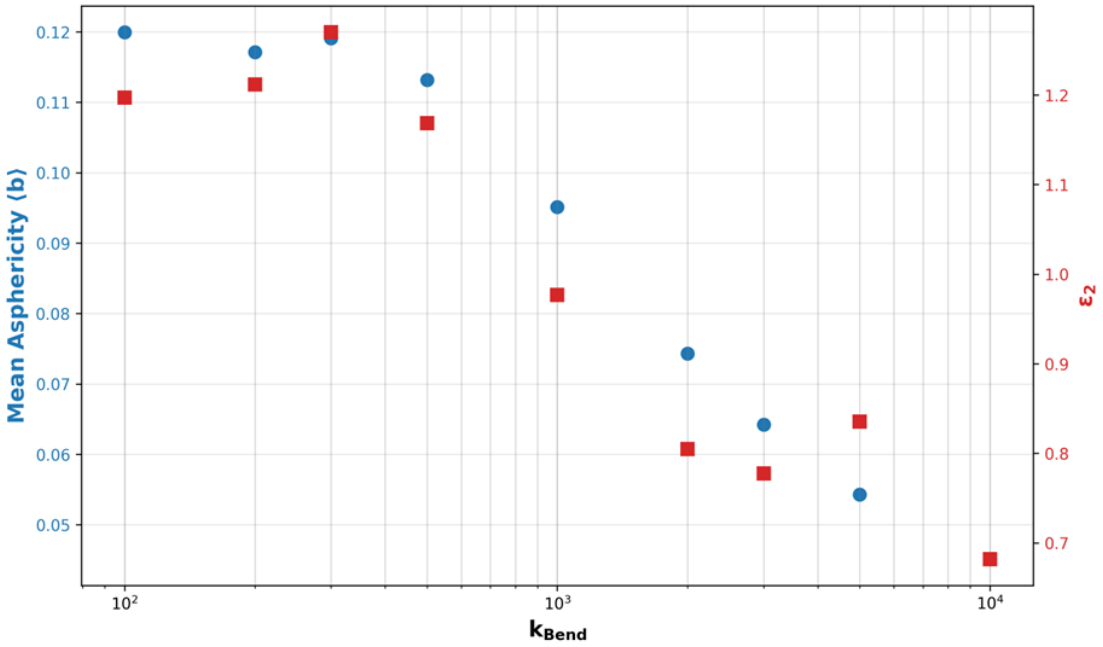

Figure 3.12.: Mean asphericity $\langle b \rangle$ (blue circles, left axis) and deformation amplitude ε_2 (red squares, right axis) as functions of bending rigidity k_{Bend} on a logarithmic scale. Both quantities decrease with increasing surface stiffness, reflecting the reduced capacity for deformation in more rigid surfaces. The bending rigidity spans two orders of magnitude from $k_{\text{Bend}} = 100$ to $k_{\text{Bend}} = 10000$.

This behavior is physically intuitive. A stiffer surface requires larger forces to achieve the same deformation, so for fixed triangle forcing parameters, increasing the bending rigidity naturally leads to smaller surface deformations. As the asphericity b approaches zero, the cell maintains a more spherical shape throughout the swimming cycle, with

the eigenvalues of the gyration tensor becoming increasingly equal. Recall that $b = 0$ corresponds to a perfect sphere, while $b > 0$ indicates deviation from spherical symmetry. Similarly, as ε_2 decreases toward zero, the surface nodes remain closer to their equilibrium positions on the reference sphere, indicating reduced deformation amplitude.

The correlated decrease of both parameters confirms their physical connection: a surface that resists bending will simultaneously exhibit reduced asphericity (staying closer to spherical) and reduced deformation amplitude (smaller displacements from equilibrium). This coupling has important implications for swimming performance, as we have established that the swimming velocity scales with ε_2^2. Consequently, stiffer surfaces are expected to produce slower swimming velocities due to their reduced capacity for the large-amplitude deformations required for efficient propulsion.

3.11. Surface Rigidity Controls Swimming Direction

Perhaps the most striking result of this investigation is the discovery that surface rigidity fundamentally determines the swimming direction. Figure 3.13 presents the mean steady-state velocity $\langle v_y \rangle$ as a function of the bending rigidity k_{Bend}, covering the same range of surface stiffness values examined previously.

The data reveal a remarkable non-monotonic behavior with a sign change. For soft surfaces at low bending rigidity ($k_{\text{Bend}} = 100$–300), the swimming velocity is positive and actually increases slightly, reaching a maximum around $k_{\text{Bend}} \approx 300$. Beyond this point, the velocity decreases rapidly, crossing zero in the range $k_{\text{Bend}} = 1000$–2000. For stiffer surfaces ($k_{\text{Bend}} > 2000$), the velocity becomes negative, indicating a reversal of swimming direction.

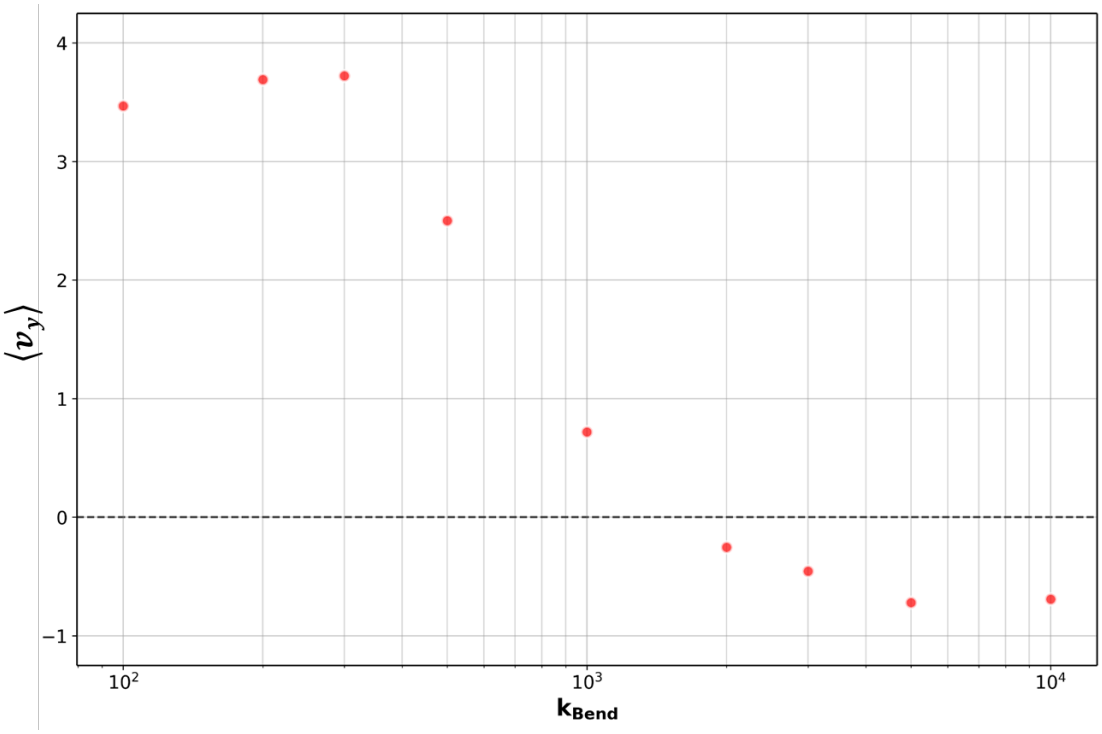

Figure 3.13.: Mean steady-state velocity $\langle v_y \rangle$ as a function of bending rigidity k_{Bend}. Soft surfaces (low k_{Bend}) exhibit forward swimming where stroking dominates, while stiff surfaces (high k_{Bend}) exhibit backward swimming where surface velocity dominates. The transition occurs between $k_{\text{Bend}} = 1000$ and 2000, demonstrating that surface rigidity controls swimming direction.

This transition between forward and backward swimming can be understood in terms of two competing propulsion mechanisms. For soft surfaces with low k_{Bend}, the surface undergoes large-amplitude non-reciprocal deformations, and the stroking motion dominates the propulsion. The resulting shape changes effectively push fluid backward, propelling the

cell forward. In contrast, for stiff surfaces with high k_{Bend}, the surface resists deformation and the surface velocity contribution becomes dominant. In this regime, the fluid-surface interaction produces a net backward motion of the cell.

The existence of a well-defined transition region between $k_{\text{Bend}} = 1000$ and $k_{\text{Bend}} = 2000$ suggests a crossover where neither mechanism dominates, resulting in near-zero net displacement. This finding has significant implications for understanding biological microswimmers and designing synthetic micro-robots: by tuning the surface stiffness, one can control not only the swimming speed but also the swimming direction, enabling bidirectional locomotion with a single actuation mechanism.

4. Conclusion and Outlook

4.1. Summary of Results

This thesis presented a computational study of deformable cell swimming at low Reynolds numbers using coupled Molecular Dynamics and Multi-Particle Collision Dynamics simulations. By modeling the cell membrane as a triangulated elastic surface immersed in an MPCD fluid, we investigated how surface mechanical properties govern locomotion through non-reciprocal surface deformations.

The central finding of this work is that surface bending rigidity acts as a control parameter that determines not only swimming speed but also swimming direction. For soft surfaces with low bending rigidity ($k_{\mathrm{Bend}} < 1000$), the cell exhibits forward swimming where stroking-dominated propulsion prevails. In this regime, large-amplitude surface deformations effectively push fluid backward, generating forward thrust. For stiff surfaces ($k_{\mathrm{Bend}} > 2000$), the swimming direction reverses: the surface resists large deformations, and surface velocity contributions dominate, resulting in net backward motion. The transition between these regimes occurs in a well-defined range ($k_{\mathrm{Bend}} = 1000$–2000), where the two competing mechanisms approximately balance and the net displacement approaches zero.

We further demonstrated that the swimming velocity obeys the canonical microswimmer scaling relation $v \propto \varepsilon_2^2 f$, where ε_2 characterizes the deformation amplitude and f is the driving frequency. This quadratic dependence on amplitude, validated with a correlation coefficient of $R^2 = 0.9775$, confirms that our deformable swimmer operates according to the fundamental principles established for low Reynolds number locomotion. The agreement with theoretical predictions provides confidence that the simulation framework captures the essential physics of viscous swimming.

The parametric study of bending rigidity also revealed a direct coupling between surface stiffness, deformation amplitude, and cell shape. As k_{Bend} increases, both the asphericity b and the deformation parameter ε_2 decrease systematically. Stiffer surfaces maintain more spherical configurations throughout the swimming cycle and exhibit smaller displacements from the equilibrium shape. Since swimming velocity scales with ε_2^2, this coupling implies that increasing surface rigidity reduces swimming efficiency through two mechanisms: directly by shifting the propulsion mode toward backward swimming, and indirectly by suppressing the deformation amplitude required for efficient stroking.

4.2. Limitations of the Present Model

While the simulation framework successfully captures essential features of deformable cell swimming, several simplifications limit its direct applicability to biological systems.

The triangulated surface model employs a fixed mesh topology throughout the simulation. In contrast, real biological membranes are fluid: lipid molecules can diffuse laterally within the bilayer, and the membrane can undergo topological rearrangements. This membrane fluidity, sometimes modeled through bond-flipping algorithms that dynamically reassign mesh connectivity, is absent in our approach. Consequently, the model cannot capture phenomena such as membrane flow around the cell or topology-dependent shape transitions that may be relevant for certain biological swimmers.

The spatial discretization with approximately 1000 surface nodes represents a relatively coarse approximation of a continuous membrane. While sufficient to resolve the global deformation modes relevant for swimming, finer discretization would be required to capture small-scale surface features or to investigate phenomena occurring at length scales comparable to the mesh spacing.

The actuation mechanism, based on periodic forces applied to three triangle vertices, represents a highly simplified abstraction of biological propulsion mechanisms. Real cells employ diverse strategies including ciliary beating, flagellar rotation, and cortical contractions driven by complex biochemical machinery. Our model isolates the mechanical aspects of non-reciprocal deformation but does not address the biological regulation of such deformations.

Finally, the present analysis is based on approximately ten complete swimming cycles. While sufficient to establish steady-state behavior and extract mean swimming velocities, longer simulations would provide better statistics and enable investigation of long-time diffusive behavior or rare fluctuation events.

4.3. Outlook and Future Directions

Several directions for future research emerge naturally from this work.

Extended simulations over many more swimming cycles would improve statistical accuracy and enable characterization of velocity fluctuations, orientational diffusion, and long-time transport properties. Such studies could reveal whether the swimmer exhibits anomalous diffusion or develops correlations over extended time scales.

The influence of cell geometry on swimming performance remains largely unexplored. Initializing the simulation with non-spherical shapes such as prolate or oblate ellipsoids, or investigating how the location and configuration of the driving triangle affects propulsion, could reveal design principles for optimizing swimming efficiency.

Comparison with experimental measurements on biological microswimmers or synthetic deformable particles would provide crucial validation of the model predictions. Mapping the simulation parameters to physical quantities such as membrane bending moduli measured in micropipette aspiration experiments or swimming velocities observed in microscopy studies would establish the quantitative accuracy of the approach and guide refinement of the model.

The discovery that membrane rigidity controls swimming direction suggests intriguing possibilities for designing controllable microswimmers. A synthetic swimmer with tunable surface stiffness, achieved for example through responsive polymers or active materials, could potentially switch between forward and backward locomotion without changing its actuation pattern. Exploring such design concepts through simulation could inform experimental efforts in micro-robotics and targeted drug delivery.

Incorporating more realistic membrane physics, including membrane fluidity through bond-flipping dynamics or explicit treatment of the lipid bilayer structure, would extend the model toward greater biological fidelity. Similarly, coupling the mechanical model to biochemical reaction networks that regulate actuation could enable investigation of feedback mechanisms in biological cell motility.

In conclusion, this thesis establishes a computational framework for studying deformable cell swimming and demonstrates that membrane mechanical properties play a central role in determining locomotion characteristics. The finding that bending rigidity controls swimming direction opens new perspectives for understanding biological microswimmers and designing synthetic micro-robots with controllable motility.

List of Figures

List of Software and Tools

The following table lists the digital tools, software, and services that were used in support of this thesis. The author retains full responsibility for the content and the independent development of all scientific work.

Tool / Software / Service	**Used in**	**Purpose of Use**
Claude (Anthropic)	Entire thesis	Assistance with phrasing, structure, stylistic revision, and code development support. Full content responsibility remains with the author.
Visual Studio Code	Code development	Editor for Python and Fortran code, including terminal use
Python	Data analysis	Programming language for data processing, visualization, and plotting
Fortran	Simulations	Programming language for implementing and running the MD/MPCD simulation code
Vienna Scientific Cluster (VSC)	Simulations	Execution of numerical simulations on the Austrian high-performance computing infrastructure
LaTeX	Entire document	Typesetting system for producing the written thesis
Overleaf	Thesis writing	Online LaTeX editor for collaborative writing and compilation
Google Sheets	Project management	Documentation of simulation parameters and results tracking
Google Docs	Note taking	Collection of notes and drafts during the research process

Overview of tools, software, and services used in this thesis.

Bibliography

[1] A. D. Luster, R. Alon and U. H. von Andrian, 'Immune cell migration in inflammation: Present and future therapeutic targets', *Nature Immunology*, vol. 6, no. 12, pp. 1182–1190, 2005. DOI: 10.1038/ni1275.

[2] M. F. Krummel, F. Bartumeus and A. Gérard, 'T cell migration, search strategies and mechanisms', *Nature Reviews Immunology*, vol. 16, no. 3, pp. 193–201, 2016. DOI: 10.1038/nri.2015.16.

[3] J. Winkler, A. Abisoye-Ogunniyan, K. J. Metcalf and Z. Werb, 'Concepts of extracellular matrix remodelling in tumour progression and metastasis', *Nature Communications*, vol. 11, p. 5120, 2020. DOI: 10.1038/s41467-020-18794-x.

[4] F. Kai, E. Bhathena, D. Bhatt and V. Sharma, 'Extracellular matrix mechanobiology in cancer cell migration', *Acta Biomaterialia*, vol. 163, pp. 66–84, 2023. DOI: 10.1016/j.actbio.2022.09.071.

[5] P. Friedl, S. Borgmann and E.-B. Bröcker, 'Amoeboid leukocyte crawling through extracellular matrix: Lessons from the Dictyostelium paradigm of cell movement', *Journal of Leukocyte Biology*, vol. 70, no. 4, pp. 491–509, 2001.

[6] N. P. Barry and M. S. Bretscher, 'Dictyostelium amoebae and neutrophils can swim', *Proceedings of the National Academy of Sciences*, vol. 107, no. 25, pp. 11 376–11 380, 2010. DOI: 10.1073/pnas.1006327107.

[7] E. A. Gaffney, H. Gadêlha, D. J. Smith, J. R. Blake and J. C. Kirkman-Brown, 'Mammalian sperm motility: Observation and theory', *Annual Review of Fluid Mechanics*, vol. 43, pp. 501–528, 2011. DOI: 10.1146/annurev-fluid-121108-145442.

[8] H. C. Berg, *E. coli in Motion*. New York: Springer, 2004, ISBN: 978-0387008882.

[9] N. Wadhwa and H. C. Berg, 'Bacterial motility: Machinery and mechanisms', *Nature Reviews Microbiology*, vol. 20, no. 3, pp. 161–173, 2022. DOI: 10.1038/s41579-021-00626-4.

[10] K. Bouhouche, A. Gupte, R. Le Borgne, M. Laady, N. Fiditi, E. Culetto, J. Cohen, R. P. S. Bhullar, R. P. Bhullar, R. P. S. Bhullar, R. P. S. Bhullar and R. P. S. Bhullar, 'Paramecium, a model to study ciliary beating and ciliogenesis', *Frontiers in Cell and Developmental Biology*, vol. 10, p. 847 908, 2022. DOI: 10.3389/fcell.2022.847908.

[11] N. Osterman and A. Vilfan, 'Finding the ciliary beating pattern with optimal efficiency', *Proceedings of the National Academy of Sciences*, vol. 108, no. 38, pp. 15 727–15 732, 2011. DOI: 10.1073/pnas.1107889108.

[12] M. Lisicki, M. F. Velho Rodrigues, R. E. Goldstein and E. Lauga, 'The bank of swimming organisms at the micron scale (BOSO-Micro)', *PLOS ONE*, vol. 16, no. 6, e0252291, 2021. DOI: 10.1371/journal.pone.0252291.

[13] R. Milo and R. Phillips, *Cell Biology by the Numbers*. New York: Garland Science, 2015, ISBN: 978-0815345374.

[14] X. Trepat, Z. Chen and K. Jacobson, 'Cell migration', *Comprehensive Physiology*, vol. 2, no. 4, pp. 2369–2392, 2012. DOI: 10.1002/cphy.c110012.

[15] E. Lauga, 'Bacterial hydrodynamics', *Annual Review of Fluid Mechanics*, vol. 48, pp. 105–130, 2016. DOI: 10.1146/annurev-fluid-122414-034606.

[16] L. D. Landau and E. M. Lifshitz, *Fluid Mechanics*, 2nd ed., ser. Course of Theoretical Physics. Pergamon Press, 1987, vol. 6, ISBN: 978-0-08-033933-7. DOI: 10.1016/C2013-0-03799-1.

[17] E. M. Purcell, 'Life at low Reynolds number', *American Journal of Physics*, vol. 45, no. 1, pp. 3–11, 1977. DOI: 10.1119/1.10903.

[18] J. Happel and H. Brenner, *Low Reynolds Number Hydrodynamics: With Special Applications to Particulate Media*, 1st ed., ser. Mechanics of Fluids and Transport Processes. Springer Netherlands, 1983, vol. 1. DOI: 10.1007/978-94-009-8352-6.

[19] E. Lauga and T. R. Powers, 'The hydrodynamics of swimming microorganisms', *Reports on Progress in Physics*, vol. 72, no. 9, p. 096 601, Aug. 2009. DOI: 10.1088/0034-4885/72/9/096601.

[20] M. J. Lighthill, 'On the squirming motion of nearly spherical deformable bodies through liquids at very small reynolds numbers', *Communications on Pure and Applied Mathematics*, vol. 5, pp. 109–118, 1952. [Online]. Available: https://api.semanticscholar.org/CorpusID:121155076.

[21] J. R. Blake, 'A spherical envelope approach to ciliary propulsion', *Journal of Fluid Mechanics*, vol. 46, no. 1, pp. 199–208, 1971. DOI: 10.1017/S002211207100048X.

[22] A. Shapere and F. Wilczek, 'Geometry of self-propulsion at low Reynolds number', *Journal of Fluid Mechanics*, vol. 198, pp. 557–585, 1989. DOI: 10.1017/S002211208900025X.

[23] A. Shapere and F. Wilczek, 'Self-propulsion at low Reynolds number', *Physical Review Letters*, vol. 58, pp. 2051–2054, 20 May 1987. DOI: 10.1103/PhysRevLett.58.2051.

[24] S. Dinas and J. Bañón, 'A review on Delaunay triangulation with application on computer vision', *International Journal of Computer Science and Engineering*, vol. 3, pp. 9–18, 2014.

[25] J. T. Bachmann, 'Brownian dynamics simulations of driven deformable cells in ordered polymer networks', Master of Science Thesis, University of Vienna, 2022.

[26] M. Peltomäki and G. Gompper, 'Sedimentation of single red blood cells', *Soft Matter*, vol. 9, p. 8346, 2013. DOI: 10.1039/c3sm50592h.

[27] A. Guckenberger and S. Gekle, 'Theory and algorithms to compute helfrich bending forces: A review', *Journal of Physics: Condensed Matter*, vol. 29, no. 20, p. 203 001, 2017. DOI: 10.1088/1361-648X/aa6313.

[28] A. Guckenberger, M. Schraml, P. Chen, M. Leonetti and S. Gekle, 'On the bending algorithms for soft objects in flows', *Computer Physics Communications*, vol. 207, pp. 1–23, 2016, ISSN: 0010-4655. DOI: 10.1016/j.cpc.2016.04.018. [Online]. Available: https://www.sciencedirect.com/science/article/pii/S0010465516301072.

[29] M. S. Rizvi, A. Farutin and C. Misbah, 'Three-bead steering microswimmers', *Physical Review E*, vol. 97, p. 023 102, 2 Feb. 2018. DOI: 10.1103/PhysRevE.97.023102. [Online]. Available: https://link.aps.org/doi/10.1103/PhysRevE.97.023102.

[30] A. Malevanets and R. Kapral, 'Mesoscopic model for solvent dynamics', *Journal of Chemical Physics*, vol. 110, no. 17, pp. 8605–8613, 1999. DOI: 10.1063/1.478857.

[31] A. Malevanets and R. Kapral, 'Mesoscopic model for solvent dynamics', *Journal of Chemical Physics*, vol. 112, no. 14, pp. 7260–7269, 2000. DOI: 10.1063/1.481289.

[32] G. Gompper, T. Ihle, D. M. Kroll and R. G. Winkler, 'Multi-particle collision dynamics—a particle-based mesoscale simulation approach to the hydrodynamics of complex fluids', *Advances in Polymer Science*, vol. 221, pp. 1–87, 2009. DOI: 10.1007/978-3-540-87967-1_1.

[33] R. Kapral, 'Multiparticle collision dynamics: Simulation of complex systems on mesoscales', *Advances in Chemical Physics*, vol. 140, pp. 89–146, 2008. DOI: 10.1002/9780470371572.ch2.

[34] J. T. Padding and A. A. Louis, 'Hydrodynamic interactions and brownian forces in colloidal suspensions: Coarse-graining over time and length scales', *Phys. Rev. E*, vol. 74, p. 031 402, 2006.

[35] E. Allahyarov and G. Gompper, 'Mesoscopic solvent simulations: Multiparticle-collision dynamics of three-dimensional flows', *Physical Review E*, vol. 66, no. 3, p. 036 702, 2002. DOI: 10.1103/PhysRevE.66.036702.

[36] A. Zöttl and H. Stark, 'Emergent behavior in active colloids', *Journal of Physics: Condensed Matter*, vol. 28, no. 25, p. 253 001, 2016. DOI: 10.1088/0953-8984/28/25/253001.

[37] H. Noguchi and G. Gompper, 'Dynamics of fluid vesicles in shear flow: Effect of membrane viscosity and thermal fluctuations', *Physical Review E*, vol. 72, p. 011 901, 1 2005. DOI: 10.1103/PhysRevE.72.011901. [Online]. Available: https://link.aps.org/doi/10.1103/PhysRevE.72.011901.

[38] S. Babu and H. Stark, 'Dynamics of semi-flexible tethered sheets', *European Physical Journal E*, vol. 34, p. 136, 2011. DOI: 10.1140/epje/i2011-11136-2.

[39] D. C. Rapaport, *The Art of Molecular Dynamics Simulation*, 2nd ed. Cambridge University Press, 2004.

[40] A. R. Leach, *Molecular Modeling: Principles and Applications*, 2nd ed. Pearson Education Limited, 2001.

[41] G. Gompper, T. Ihle, D. Kroll and R. Winkler, 'Multi-particle collision dynamics: A particle-based mesoscale simulation approach to the hydrodynamics of complex fluids', in *Advanced Computer Simulation Approaches for Soft Matter Sciences III*, ser. Advances in Polymer Science, C. Holm and K. Kremer, Eds., vol. 221, Springer, Berlin, Heidelberg, 2009. DOI: 10.1007/978-3-540-87706-6_1.

[42] H. C. Andersen, 'Molecular dynamics simulations at constant pressure and/or temperature', *The Journal of Chemical Physics*, vol. 72, no. 4, pp. 2384–2393, 1980. DOI: 10.1063/1.439486.

[43] R. J. Renka, 'Algorithm 772: STRIPACK: Delaunay triangulation and Voronoi diagram on the surface of a sphere', *ACM Transactions on Mathematical Software*, vol. 23, no. 3, pp. 416–434, 1997. DOI: 10.1145/275323.275329.

[44] G. Marsaglia and W. W. Tsang, 'The ziggurat method for generating random variables', *Journal of Statistical Software*, vol. 5, no. 8, pp. 1–7, 2000. DOI: 10.18637/jss.v005.i08.

[45] E. Anderson, Z. Bai, C. Bischof *et al.*, *LAPACK Users' Guide*, 3rd. Philadelphia: SIAM, 1999.

[46] L. Verlet, 'Computer "experiments" on classical fluids. I. Thermodynamical properties of Lennard-Jones molecules', *Physical Review*, vol. 159, no. 1, pp. 98–103, 1967. DOI: 10.1103/PhysRev.159.98.

[47] W. C. Swope, H. C. Andersen, P. H. Berens and K. R. Wilson, 'A computer simulation method for the calculation of equilibrium constants for the formation of physical clusters of molecules: Application to small water clusters', *The Journal of Chemical Physics*, vol. 76, no. 1, pp. 637–649, 1982. DOI: 10.1063/1.442716.

[48] C. R. Harris, K. J. Millman, S. J. van der Walt *et al.*, 'Array programming with NumPy', *Nature*, vol. 585, pp. 357–362, 2020. DOI: 10.1038/s41586-020-2649-2.

[49] J. D. Hunter, 'Matplotlib: A 2d graphics environment', *Computing in Science & Engineering*, vol. 9, no. 3, pp. 90–95, 2007. DOI: 10.1109/MCSE.2007.55.

[50] J. S. Guasto, K. A. Johnson and J. P. Gollub, 'Oscillatory flows induced by microorganisms swimming in two dimensions', *Phys. Rev. Lett.*, vol. 105, p. 168 102, 2010.

A. Selected Code Implementations

This appendix presents selected Fortran subroutines from the simulation code that implement the core algorithms discussed in this thesis. The complete simulation framework is based on the SPICCE (Simulation Package for Investigating Cells in Complex Environments) codebase developed by Bachmann [25].

A.1. Triangle Active Force

The following subroutine implements the time-dependent active forces applied to the triangle nodes for non-reciprocal deformation. Forces are applied along the connecting vectors between nodes with sinusoidal time dependence and phase shifts.

```
SUBROUTINE tr_compr_force(N_nodes, positions, cf, T, F_compress, &
   & a1, a2, g, nodelist, delta_t, count_mpcd, epsilon, PI, &
   & terminal_updates)

   IMPLICIT NONE

   ! DECLARATIONS
   INTEGER :: N_nodes                          ! number of membrane nodes
   DOUBLE PRECISION :: positions(N_nodes,3)    ! node position vectors
   DOUBLE PRECISION :: vector_12(3)            ! vector from node 1 to 2
   DOUBLE PRECISION :: vector_23(3)            ! vector from node 2 to 3
   DOUBLE PRECISION :: vector_31(3)            ! vector from node 3 to 1

   ! COMPRESSION PARAMETERS
   DOUBLE PRECISION :: cf                      ! force amplitude
   DOUBLE PRECISION :: T                       ! compression period
   DOUBLE PRECISION :: a1                      ! phase shift 1
   DOUBLE PRECISION :: a2                      ! phase shift 2
   DOUBLE PRECISION :: g                       ! amplitude factor
   INTEGER :: nodelist(3)                      ! triangle node indices

   ! FORCES
   DOUBLE PRECISION :: F_compress(N_nodes,3)   ! compression forces

   ! TIME VARIABLES
   DOUBLE PRECISION :: delta_t
   INTEGER :: count_mpcd
   DOUBLE PRECISION :: epsilon
   REAL :: PI
   LOGICAL :: terminal_updates

   ! FORCE CALCULATION
```

```
33    F_compress = 0.0
34
35    ! Calculate connecting vectors
36    vector_12(:) = positions(nodelist(2),:) - positions(nodelist(1),:)
37    vector_23(:) = positions(nodelist(3),:) - positions(nodelist(2),:)
38    vector_31(:) = positions(nodelist(1),:) - positions(nodelist(3),:)
39
40    ! Calculate time-dependent compression forces
41    IF(T > epsilon) THEN
42       F_compress(nodelist(1),:) = &
43          &   cf * vector_12(:)/norm2(vector_12(:)) &
44          &     * SIN(2.0*PI/T * delta_t*count_mpcd) &
45          & - cf * vector_31(:)/norm2(vector_31(:)) &
46          &     * SIN(2.0*PI/T * delta_t*count_mpcd + a2)
47
48       F_compress(nodelist(2),:) = &
49          &   cf * vector_23(:)/norm2(vector_23(:)) &
50          &     * SIN(2.0*PI/T * delta_t*count_mpcd + a1) &
51          & - cf * vector_12(:)/norm2(vector_12(:)) &
52          &     * SIN(2.0*PI/T * delta_t*count_mpcd)
53
54       F_compress(nodelist(3),:) = &
55          &   cf * vector_31(:)/norm2(vector_31(:)) &
56          &     * SIN(2.0*PI/T * delta_t*count_mpcd + a2) &
57          & - cf * vector_23(:)/norm2(vector_23(:)) &
58          &     * SIN(2.0*PI/T * delta_t*count_mpcd + a1)
59    END IF
60
61 END SUBROUTINE tr_compr_force
```

Listing A.1: Triangle compression force subroutine for active swimming.

The force on each triangle node consists of two contributions: an attractive force along one adjacent edge and a repulsive force along the other. The sinusoidal time dependence with phase shifts α_1 and α_2 ensures non-reciprocal deformation patterns that break time-reversal symmetry.

A.2. Velocity Verlet Integration

The velocity Verlet algorithm is implemented in two separate subroutines that are called at different stages of each time step. This symplectic integrator preserves phase space volume and provides excellent energy conservation.

```
1  SUBROUTINE velocity_verlet_1(N_nodes, X, V, F_tot, mass, delta_t, &
2     & terminal_updates)
3
4     IMPLICIT NONE
5
6     ! DECLARATIONS
7     INTEGER :: N_nodes                          ! number of membrane nodes
8     DOUBLE PRECISION :: X(N_nodes,3)            ! position data
9     DOUBLE PRECISION :: V(N_nodes,3)            ! velocity data
```

```
10    DOUBLE PRECISION :: mass                  ! mass of membrane nodes
11    DOUBLE PRECISION :: F_tot(N_nodes,3)      ! total forces
12    DOUBLE PRECISION :: delta_t               ! time step
13    INTEGER :: i, j                           ! loop indices
14    LOGICAL :: terminal_updates
15
16    ! VELOCITY VERLET STEP 1: v(t+dt/2) and x(t+dt)
17    DO i = 1, N_nodes
18       DO j = 1, 3
19          V(i,j) = V(i,j) + 0.5 * delta_t * F_tot(i,j) / mass
20          X(i,j) = X(i,j) + delta_t * V(i,j)
21       END DO
22    END DO
23
24 END SUBROUTINE velocity_verlet_1
```

Listing A.2: First part of the velocity Verlet algorithm: half-step velocity update and full position update.

```
1  SUBROUTINE velocity_verlet_2(N_nodes, V, F_tot, mass, delta_t, &
2     & terminal_updates)
3
4     IMPLICIT NONE
5
6     ! DECLARATIONS
7     INTEGER :: N_nodes                        ! number of membrane nodes
8     DOUBLE PRECISION :: V(N_nodes,3)          ! velocity data
9     DOUBLE PRECISION :: mass                  ! mass of membrane nodes
10    DOUBLE PRECISION :: F_tot(N_nodes,3)      ! total forces
11    DOUBLE PRECISION :: delta_t               ! time step
12    INTEGER :: i, j                           ! loop indices
13    LOGICAL :: terminal_updates
14
15    ! VELOCITY VERLET STEP 2: v(t+dt)
16    DO i = 1, N_nodes
17       DO j = 1, 3
18          V(i,j) = V(i,j) + 0.5 * delta_t * F_tot(i,j) / mass
19       END DO
20    END DO
21
22 END SUBROUTINE velocity_verlet_2
```

Listing A.3: Second part of the velocity Verlet algorithm: completing the velocity update.

The algorithm proceeds as follows: first, velocities are updated by half a time step using the current forces (`velocity_verlet_1`). Positions are then updated using these intermediate velocities. After recalculating forces at the new positions, the velocity update is completed (`velocity_verlet_2`).

A.3. Cell-Fluid Coupling via MPCD Collision

The MPCD collision step couples the cell membrane nodes with the surrounding fluid particles through stochastic momentum exchange. This routine implements the Andersen thermostat variant that conserves momentum locally within each collision cell.

```
SUBROUTINE collision_step(r_f, v_f, m_f, n_f, r_c, v_c, m_c, n_c, &
   & box, epsilon, epsilon_lp, terminal_updates)

   USE Ziggurat
   IMPLICIT NONE

   ! FLUID PROPERTIES
   DOUBLE PRECISION, DIMENSION(n_f,3) :: r_f, v_f  ! positions/velocities
   DOUBLE PRECISION :: m_f                          ! fluid particle mass
   INTEGER n_f                                      ! number of particles
   DOUBLE PRECISION, DIMENSION(n_f,3) :: vrand_f    ! random velocities
   INTEGER, DIMENSION(n_f,3) :: ID_f                ! cell box indices
   INTEGER, DIMENSION(box(1),box(2),box(3)) :: NCell_f
   DOUBLE PRECISION, DIMENSION(box(1),box(2),box(3),3) :: vcm_f, mvrand_f

   ! CELL PROPERTIES
   DOUBLE PRECISION, DIMENSION(n_c,3) :: r_c, v_c  ! positions/velocities
   DOUBLE PRECISION :: m_c                          ! cell node mass
   INTEGER n_c                                      ! number of nodes
   DOUBLE PRECISION, DIMENSION(n_c,3) :: vrand_c    ! random velocities
   INTEGER, DIMENSION(n_c,3) :: ID_c                ! cell box indices
   INTEGER, DIMENSION(box(1),box(2),box(3)) :: NCell_c
   DOUBLE PRECISION, DIMENSION(box(1),box(2),box(3),3) :: vcm_c, mvrand_c

   ! BOX AND COMBINED QUANTITIES
   INTEGER, DIMENSION(3) :: box
   DOUBLE PRECISION, DIMENSION(box(1),box(2),box(3),3) :: v_E, u_E
   DOUBLE PRECISION, DIMENSION(3) :: a_shift
   DOUBLE PRECISION :: epsilon, epsilon_lp
   LOGICAL :: terminal_updates
   INTEGER :: i, j, dim, i1, i2, i3

   dim = 3

   ! Random grid shift for Galilean invariance
   a_shift = [uni()-0.5, uni()-0.5, uni()-0.5]

   ! Shift all positions
   DO i = 1, n_f
      r_f(i,:) = r_f(i,:) + a_shift
   END DO
   DO i = 1, n_c
      r_c(i,:) = r_c(i,:) + a_shift
   END DO

   ! Apply periodic boundary conditions
   CALL periodic_boundary_conditions(r_f, n_f, box, terminal_updates)
```

```
48
49    ! Assign particles to collision cells
50    ID_f = ceiling(r_f)
51    ID_c = ceiling(r_c)
52
53    ! Initialize accumulators
54    vcm_f = 0.0;  mvrand_f = 0.0;  NCell_f = 0
55    vcm_c = 0.0;  mvrand_c = 0.0;  NCell_c = 0
56
57    ! Accumulate fluid quantities in each collision cell
58    DO i = 1, n_f
59       vcm_f(ID_f(i,1),ID_f(i,2),ID_f(i,3),:) = &
60          & vcm_f(ID_f(i,1),ID_f(i,2),ID_f(i,3),:) + v_f(i,:)
61       Ncell_f(ID_f(i,1),ID_f(i,2),ID_f(i,3)) = &
62          & Ncell_f(ID_f(i,1),ID_f(i,2),ID_f(i,3)) + 1
63       DO j = 1, dim
64          vrand_f(i,j) = rnor() / SQRT(m_f)
65       END DO
66       mvrand_f(ID_f(i,1),ID_f(i,2),ID_f(i,3),:) = &
67          & mvrand_f(ID_f(i,1),ID_f(i,2),ID_f(i,3),:) + vrand_f(i,:)
68    END DO
69
70    ! Accumulate cell quantities in each collision cell
71    DO i = 1, n_c
72       vcm_c(ID_c(i,1),ID_c(i,2),ID_c(i,3),:) = &
73          & vcm_c(ID_c(i,1),ID_c(i,2),ID_c(i,3),:) + v_c(i,:)
74       Ncell_c(ID_c(i,1),ID_c(i,2),ID_c(i,3)) = &
75          & Ncell_c(ID_c(i,1),ID_c(i,2),ID_c(i,3)) + 1
76       DO j = 1, dim
77          vrand_c(i,j) = rnor() / SQRT(m_c)
78       END DO
79       mvrand_c(ID_c(i,1),ID_c(i,2),ID_c(i,3),:) = &
80          & mvrand_c(ID_c(i,1),ID_c(i,2),ID_c(i,3),:) + vrand_c(i,:)
81    END DO
82
83    ! Calculate mean velocities v_E and u_E for each cell
84    DO i1 = 1, box(1)
85       DO i2 = 1, box(2)
86          DO i3 = 1, box(3)
87             IF(Ncell_f(i1,i2,i3) /= 0 .OR. Ncell_c(i1,i2,i3) /= 0) THEN
88                ! Mass-weighted mean random velocity
89                v_E(i1,i2,i3,:) = 1./(m_f*Ncell_f(i1,i2,i3) &
90                   & + m_c*Ncell_c(i1,i2,i3)) &
91                   & * (m_f*mvrand_f(i1,i2,i3,:) + m_c*mvrand_c(i1,i2,i3
    ,:))
92                ! Mass-weighted center-of-mass velocity
93                u_E(i1,i2,i3,:) = 1./(m_f*Ncell_f(i1,i2,i3) &
94                   & + m_c*Ncell_c(i1,i2,i3)) &
95                   & * (m_f*vcm_f(i1,i2,i3,:) + m_c*vcm_c(i1,i2,i3,:))
96             END IF
97          END DO
98       END DO
99    END DO
```

```
100
101    ! Collision step for fluid particles
102    DO i = 1, n_f
103       v_f(i,:) = vrand_f(i,:) + u_E(ID_f(i,1),ID_f(i,2),ID_f(i,3),:) &
104                & - v_E(ID_f(i,1),ID_f(i,2),ID_f(i,3),:)
105    END DO
106
107    ! Collision step for cell nodes
108    DO i = 1, n_c
109       v_c(i,:) = vrand_c(i,:) + u_E(ID_c(i,1),ID_c(i,2),ID_c(i,3),:) &
110                & - v_E(ID_c(i,1),ID_c(i,2),ID_c(i,3),:)
111    END DO
112
113    ! Shift positions back
114    DO i = 1, n_f
115       r_f(i,:) = r_f(i,:) - a_shift
116    END DO
117    DO i = 1, n_c
118       r_c(i,:) = r_c(i,:) - a_shift
119    END DO
120
121    CALL periodic_boundary_conditions(r_f, n_f, box, terminal_updates)
122
123 END SUBROUTINE collision_step
```

Listing A.4: MPCD collision step for cell-fluid coupling (key sections).

The collision step implements the Andersen thermostat variant of MPCD: particles within each collision cell exchange momentum while conserving the total momentum of that cell. The key update rule $\mathbf{v}_i^{\text{new}} = \boldsymbol{\xi}_i + \mathbf{u}_E - \mathbf{v}_E$ replaces individual velocities with random thermal velocities $\boldsymbol{\xi}_i$ while adding back the center-of-mass velocity $\mathbf{u}_E$ and subtracting the mean random velocity $\mathbf{v}_E$ to ensure local momentum conservation. The random grid shift by vector $\mathbf{a}$ restores Galilean invariance.